

Article

High-Gain Miniaturized Multi-Band MIMO SSPP LWA for Vehicular Communications

Tale Saeidi ^{1,2,*}, Sahar Saleh ^{1,3,*}, Nick Timmons ¹, Christopher McDaid ¹,
Ahmed Jamal Abdullah Al-Gburi ⁴, Farooq Razzaz ^{5,6} and Saeid Karamzadeh ^{7,8}

- ¹ WiSAR Lab, Atlantic Technological University (ATU), Co. Donegal, F92 FC93 Letterkenny, Ireland; nick.timmons@atu.ie (N.T.); christopher.mcdaid@atu.ie (C.M.)
 - ² Electrical and Electronics Engineering Department, Faculty of Engineering and Natural Sciences, İstinye University, Istanbul 34396, Turkey
 - ³ Department of Electronics and Communications Engineering, Faculty of Engineering, Aden University, Aden 5243, Yemen
 - ⁴ Centre of Telecommunication Research and Innovation (CeTRI), Faculty of Electronics and Computer Technology and Engineering, Universiti Teknikal Malaysia Melaka, Durian Tunggal 76100, Melaka, Malaysia; ahmedjamal@ieee.org
 - ⁵ Electrical Engineering Department, College of Engineering, Prince Sattam Bin Abdulaziz University, Al-Kharj 16278, Saudi Arabia; f.kasim@psau.edu.sa
 - ⁶ Faculty of Engineering and Information Technology, Taiz University, Taiz 6803, Yemen
 - ⁷ Millimeter Wave Technologies, Intelligent Wireless System, Silicon Austria Labs (SAL), 4040 Linz, Austria; saeid.karamzadeh@silicon-austria.com
 - ⁸ Electrical and Electronics Engineering Department, Faculty of Engineering and Natural Sciences, Bahçeşehir University, Istanbul 34349, Turkey
- * Correspondence: tale.saeidi@atu.ie (T.S.); sahar.saleh@atu.ie (S.S.)

Abstract: This paper introduces a novel miniaturized, four-mode, semi-flexible leaky wave Multiple-Input Multiple-Output (MIMO) antenna specifically designed to advance vehicular communication systems. The proposed antenna addresses key challenges in 5G low- and high-frequency bands, including millimeter-wave communication, by integrating innovative features such as a periodic Spoof Surface Plasmon Polariton Transmission Line (SSPP-TL) and logarithmic-spiral-like semi-circular strip patches parasitically fed via orthogonal ports. These design elements facilitate stable impedance matching and wide impedance bandwidths across operating bands, which is essential for vehicular networks. The hybrid combination of leaky wave and SSPP structures, along with a defected wide-slot ground structure and backside meander lines, enhances radiation characteristics by reducing back and bidirectional radiation. Additionally, a naturalization network incorporating chamfered-edge meander lines minimizes mutual coupling and introduces a fourth radiation mode at 80 GHz. Compact in size ($14 \times 12 \times 0.25 \text{ mm}^3$), the antenna achieves high-performance metrics, including $S_{11} < -18.34 \text{ dB}$, dual-polarization, peak directive gains of 11.6 dBi (free space) and 14.6 dBi (on vehicles), isolation $> 27 \text{ dB}$, Channel Capacity Loss (CCL) < 3 , Envelope Correlation Coefficient (ECC) < 0.001 , axial ratio < 2.25 , and diversity gain (DG) $> 9.85 \text{ dB}$. Extensive testing across various vehicular scenarios confirms the antenna's robustness for Vehicle-to-Vehicle (V2V), Vehicle-to-Pedestrian (V2P), and Vehicle-to-Infrastructure (V2I) communication. Its exceptional performance ensures seamless connectivity with mobile networks and enhances safety through Specific Absorption Rate (SAR) compliance. This compact, high-performance antenna is a transformative solution for connected and autonomous vehicles, addressing critical challenges in modern automotive communication networks and paving the way for reliable and efficient vehicular communication systems.



Academic Editors: Sotirios K. Goudos and Valeri Mladenov

Received: 12 December 2024

Revised: 24 January 2025

Accepted: 1 February 2025

Published: 4 February 2025

Citation: Saeidi, T.; Saleh, S.; Timmons, N.; McDaid, C.; Al-Gburi, A.J.A.; Razzaz, F.; Karamzadeh, S. High-Gain Miniaturized Multi-Band MIMO SSPP LWA for Vehicular Communications. *Technologies* **2025**, *13*, 66. <https://doi.org/10.3390/technologies13020066>

Copyright: © 2025 by the authors. Licensee MDPI, Basel, Switzerland. This article is an open access article distributed under the terms and conditions of the Creative Commons Attribution (CC BY) license (<https://creativecommons.org/licenses/by/4.0/>).

Keywords: vehicular communication; 5G; mm-wave; SSPP; MIMO LWA; circular polarization

1. Introduction

Effective vehicular communication (VC) systems are essential for road safety, emergency response, and traffic management, enabling rapid information exchange [1]. Intelligent Transportation Systems (ITS) and Vehicular ad hoc networks (VANETs) enhance connectivity and message delivery for timely alerts. Vehicular-to-everything (V2X) communication covers V2V, V2I, V2P, and V2N [2]. The mm-wave 5G band plays a key role in V2X within the Dedicated Short-Range Communication (DSRC) standard, offering high-bandwidth channels and gigabit data rates. This ensures reliable, low-latency communication for safety applications like collision avoidance and emergency alerts, even in dense urban areas. High-frequency bands with short wavelengths also improve security by making it harder for unauthorized interception or jamming [3,4].

Millimeter-wave (mm-wave) communication offers promising benefits for high-speed V2I on the Internet of Vehicles, addressing data rate and delay challenges [3]. However, its limited range, susceptibility to obstructions, environmental sensitivity, and high path loss create significant challenges in fast-moving vehicular scenarios. High-gain, narrow-beam antennas are needed to mitigate these issues, but the lack of mm-wave channel models complicates signal detection in high-mobility contexts. Multi-band antennas combining lower and mm-wave frequencies are ideal for balancing performance and overcoming these limitations [5,6].

Combining sub-6 GHz and mm-wave 5G technologies is critical for achieving low latency, supporting existing services, and enabling new capabilities. Integrating mm-wave and non-mm-wave antennas is recommended to meet consumer demands and align with wireless advancements. Affordable, compact, wideband antennas are essential for 5G, which surpasses 3G and 4G by offering faster data rates, improved service quality, reduced costs, smaller devices, and better compatibility [7]. High-gain, efficient antennas are crucial to address mm-wave frequencies' high path loss [8]. Compact antennas designed for vehicle surfaces, such as windshields or roofs, avoid issues with thick glass [9]. For effective V2X communication, broad angular coverage and polarization diversity are necessary, achieved using phased array or lens antennas. However, challenges include beam misalignment due to vehicle movement, large lens sizes, expensive phase shifters, signal loss, and side-lobe interference [10]. Dual and circular polarizations, achievable through feeding the orthogonal modes of patch antennas, offer a practical solution for reliable and efficient vehicular communications.

Vehicular antennas must meet strict standards. They have to integrate smoothly into vehicle designs, be compatible with current systems, and remain affordable to produce. The exact specifications vary by application, such as V2V, V2I, and V2P communications. These antennas must cover bands of 5.855–5.925 GHz for V2V (DSRC/ITS-G5), 5.9 GHz for V2V and V2I, and broader ranges like 2.2–3.8 GHz for lower 5G, and 24–28 GHz, 37–40 GHz for higher 5G as well as mm-wave communication applications. Polarization is key, with linear polarization (LP) suited for direct line-of-sight links, while circular polarization (CP) with an AR under 3 dB provides improved resistance to multipath interference in dynamic environments. A low AR minimizes signal degradation caused by environmental reflections. Wideband or multi-band support is crucial for effective communication. High radiation efficiency (80–90%) and adequate gain are vital for reliable performance, with typical gains of 3.7 dBi for V2V and 7–8 dBi for satellite and 5G communications. These characteristics ensure optimal performance in modern vehicular communication systems [11–13].

1.1. Current Developments and Novel Contributions of the Study

The 5G mm-wave band, alongside low-band 5G, enhances transportation safety and communication and reduces congestion. A multi-beam, multi-polarized MIMO system described in [14] operates at sub-6 GHz (2.45, 2.6, 3.4 GHz for WLAN, LTE, and 5G) and 28 GHz (26–29 GHz). The system features eight elements (four vertical, four horizontal) with tapered slot and dipole antennas sharing a single aperture. These elements, arranged on circular and cross-shaped substrates, achieve 360-degree horizontal coverage and are mounted on a 200 mm circular metal plate, simulating a vehicle rooftop. This MIMO antenna demonstrated high isolation (>15 dB) and peak gains of 3.6–4.5 dBi for sub-6 GHz and 9.1–9.8 dBi for mm-wave bands. However, the large size limits its practicality for vehicular use, and its polarization properties are not ideal. Additionally, fabrication challenges and real-world environmental testing remain unaddressed, indicating further research is needed in vehicular antenna systems [15].

Many studies have focused on antennas covering both low and high bands for vehicular communication. For example, a shared aperture design was used to combine sub-6 GHz and mm-wave 5G bands, ensuring a compact structure. In [16], a wide bandwidth (5.30–8.08 GHz) magneto-electric dipole antenna and a 28 GHz 5G band (27.15–29.02 GHz) parallel-plate resonator antenna (PPRA) were designed in a shared aperture to provide broad coverage and high data rates, making them suitable for V2V communication. The antennas achieved a gain of under 9 dBi with a compact profile but lacked key MIMO features like ECC DG, and they were tested solely for V2V communications. In [17], a compact dual-band antenna (3.38–3.64 GHz and 26.64–29.8 GHz) was designed using a multi-layer shared aperture. It included a two-element perforated patch MIMO antenna and a four-element patch beam-steering array with 1×2 subarrays. The design utilized Substrate-Integrated Waveguide Vertical Power Divider (SIWVPD) structures for efficient space use, high isolation, and independent element feeding, enabling beam steering. The proposed (26.64–29.8 GHz) array supported beam scanning of $\pm 30^\circ$ in the H-plane (with 0° and 25° angles achieved by controlling the phase of the divider). Despite a gain of nearly 7 dBi, it was low for the antenna's size, with no polarization assessment and only ECC evaluated for the MIMO antenna. In [18], a compact, single-layer wide bandwidth dual-band antenna covering 5.74–5.96 GHz and 26.66–29.72 GHz was achieved using a shared-aperture design. The SIW slotted cavity antenna was employed to address the high loss and low efficiency. The antennas provided gains of 10.8 dBi and 13.7 dBi, respectively, while maintaining side-lobe levels (SLLs) below -14.8 dB and high isolation of 45 dB. Despite achieving high gain with a large size of 88 mm^2 , the antenna did not meet all the necessary MIMO antenna diversity requirements, and its structure was relatively complex. A wide-angle narrowband leaky-wave antenna (LWA) was proposed in [19] using a SIW-SSPP structure. When slots are periodic on the SIW's top and bottom surfaces, introducing the SSPP mode, alteration on the top allows bidirectional LWA radiation. Asymmetrical slot designs resolved the OSB issue, achieving a scanning range of -60° to $+63^\circ$ from 10.5–12.5 GHz. Adding periodic truncation slits in the SSPP waveguide created three distinct frequency regions. The SSPP mode transitioned to a spatial wave in the radiation frequency range, enabling a double-port LWA with beam-sweeping functionality. While it achieved under 10 dBi gain with a 20 cm length, its size poses integration challenges in vehicles, and diversity performance was not assessed [19]. An antenna with one port was created by proportionally separating the dual-port design. It offered low-profile beam steering, enhanced directivity, 5 GHz of BW, and up to 93% radiation efficiency [20]. However, despite these advantages, the gain was not particularly impressive, given the large length of nearly 180 mm.

In [21], a multi-layer three bands antenna was designed for independent telematics in vehicles, covering 5.85–5.97 GHz, 27.6–28.5 GHz, and 131.91–155.88 GHz. The design featured a 2×2 patch array with a T-junction power divider, a quarter-wave patch element, and an 8×8 series-fed array, achieving gains of 5–6 dBi, 10.1–12 dBi, and simulated 15.1–19.8 dBi. Although it supported multi-band operation, it lacked polarization and diversity analysis and had a complex structure. In [22], a T-shaped two-element MIMO antenna for mm-wave (26.5–38.2 GHz) vehicular communication achieved a 7.11 dBi gain and 13 dB isolation. A defective ground structure (DGS) improved bandwidth and impedance matching, while CSRR enhanced bandwidth and gain. It showed an ECC < 0.005 and a DG of ~10, but polarization analysis was not performed.

Glass-mounted antennas provide a cost-effective alternative to vehicle-mounted ones, though glass's lossy nature can impact performance. Several CPW-fed monopole antennas have been designed for vehicular communication, operating at 24.6–30 GHz [15], 26–30 GHz [23], 24.1–31.0 GHz [24], and 24–29.5 GHz [25]. These designs use copper film adhered to thick glass with thermosetting adhesive, avoiding imperfections and conductivity issues from screen printing. CPW feeding reduces pattern degradation since it eliminates the need for ground on the opposite side. In [15], parasitic elements and a lattice-structure reflector with multiple patches improved boresight gain and minimized radiation distortion. A 4×1 monopole array in [23] achieved a 5.1 dBi gain and an HPBW of 11.5° with a 4×4 array. The design in [24] used a linearly polarized patch director and a grid-slotted reflector to focus fields, boosting gain to 6.2 dBi. However, these antennas suffered from low radiation efficiency due to the thick glass substrate, highlighting the need for optimized designs to overcome such limitations, as shown in Table 1.

Table 1. Comparison of the performance of latest studies on antennas for vehicular communications across lower and higher frequency bands.

Ref.	Antenna Type	f_r (GHz)	Dims. (mm \times mm)	Peak Gain (dBi)	Ports	Planar/Non-Planar	Single/Multi-Band	Vehicular Comm. Type
[14]	Dipole and slot Monopole, parasitic elements	2.5, 2.6, 3.4, 28	60 Diameter	9.8	8	Non-planar	Multi-band	5G-V2X
[15]		24.6–30	$25 \times 25 \times 3.2$	2	One	Planar	Single band	Vehicle Window Glass
[16]	Magneto electric (ME) dipole	5.9, 28	30×20	8.46	2	Planar	Dual	5G V2V
[17]	Shared-aperture stack	3.5, 28	$33 \times 23 \times 3.5$	13.6	8	Planar	Dual	mm-wave 5G
[18]	Patch/SIW cavity	5.9, 28	$52 \times 52 \times 0.77$	13.7	2	Planar	Dual	V2X
[21]	Stacked patch	27.6–28.8 131.9–137.6, 140.5–146.9, 153.1–155.9	$28.8 \times 27.3 \times 2.1$	19.8	3	planar	Triple	DSRC, 5G, 6G
[22]	Patch, DGS, and CSRR	26.5–38.2	$12 \times 25.4 \times 0.8$	7.11	2	planar	Single	5G V2X
[23]	Patch, parasitic elements	26–30	$50 \times 50 \times 3.2$	5	4	Planar	Single	Vehicle Window Glass
[24]	Patch, parasitic elements	24.1–31	$25 \times 25 \times 3.2$	6.2	1	Planar	Single	Vehicle Window Glass

Apart from discussing and investigating the recent related antennas designed for VCs, it will be informative to include recent advancements in secure and efficient authenticated key management for UAV-assisted IoVs and lightweight authentication and privacy-preserving aggregation for blockchain-enabled federate learning in VANETs. Then, explain how the proposed antenna's characteristics can help to improve the VCs.

Integrating advanced antenna designs with robust security mechanisms is crucial for enhancing vehicular communication (VC) systems. The proposed SSPP-TL MIMO LWA antenna, with multi-band operation, high gain, and beam-steering capabilities, aims to improve VCs by supporting secure and reliable links in dynamic environments. Re-

cent advancements highlight complementary solutions: a key management scheme for UAV-assisted Internet of Vehicles (IoVs) ensures secure communication through authenticated session keys, addressing dynamic network topology and resource constraints [26]. Blockchain-enabled federated learning employs lightweight authentication for secure and privacy-preserving data aggregation in Vehicular Ad Hoc Networks (VANETs), ensuring only legitimate vehicle participation [27]. Efficient cryptographic operations in UAV-ground station communication schemes enable secure, swift key establishment despite resource limitations [28]. Additionally, authentication protocols emphasize low computational overhead and privacy preservation in vehicle-to-vehicle and vehicle-to-infrastructure communications, while drone networks benefit from privacy-preserving key agreements. These advancements align with the antenna's features, fostering secure and efficient VC systems [29,30]. The proposed SSPP-TL MIMO LWA antenna design offers significant enhancements in security and reliability for UAV and vehicular communication networks by addressing critical requirements such as multi-band operation, beam-steering, and high radiation efficiency. Its broadside radiation patterns and peak gains of 11.6 dBi in the air and 14.5 dBi on vehicles ensure robust signal transmission, reducing vulnerabilities to communication failures or eavesdropping. By supporting dynamic link optimization through SSPP periodic arrays and spiral parasitic structures, the antenna facilitates secure authenticated key management for UAV-assisted IoVs. Multi-band operation across 23.67–27.26 GHz and 71.8–82.5 GHz ensures uninterrupted connectivity for blockchain-enabled federated learning in VANETs, while high efficiency (91–93%) and minimal interference enhance UAV-to-UAV and vehicle-to-infrastructure communications. Additionally, its adaptability to vehicular placements and strong far-field patterns improves privacy-preserving protocols. These attributes make the antenna a robust solution for secure, high-performance UAV and vehicular communication systems.

Integrating diffractive neural networks (D2NNs) into the SSPP-TL MIMO LWA antenna system revolutionizes communication performance and adaptability. D2NNs use diffractive optical layers and programmable plasmonic surfaces for real-time, passive, and efficient electromagnetic signal processing. These features align with the multi-band, compact, and beam-steering capabilities of SSPP-TL MIMO LWA [31,32]. In dynamic vehicular communication scenarios, D2NNs optimize radiation patterns and beam-steering configurations to mitigate interference and multipath propagation. By processing incident signals through trained layers, they enable real-time adjustments, ensuring robust connectivity with vehicles, pedestrians, roadside units, and mobile networks. Their passive nature enhances energy efficiency compared to traditional methods while maintaining compactness. D2NNs also optimize electromagnetic exposure, complying with SAR regulations by minimizing radiation exposure without sacrificing performance. Their programmability allows adaptability to future advancements in 5G and beyond, enabling precise multi-directional and multi-band communication. This hybrid system, combining SSPP periodic arrays, leaky-wave structures, and D2NN computational intelligence, provides a compact, high-performance, and adaptive solution for modern vehicular communication networks.

1.2. Paper's Contributions

Overcoming the challenges of the recent articles shown in Table 1, this work improves VCs by offering a miniaturized, multi-frequency, dual-polarization semi-flexible antenna. It also tackles recent antennas' limitations for VCs, such as having lower gain, poorer radiation efficiency, bulky designs, single polarization, narrow bandwidth, and limited data rates. Unlike prior research, this article considers the vehicle's full-body impact on antenna performance and evaluates the SAR for safety and compliance with electromagnetic exposure standards. The effects of the vehicle body on antenna performance are entirely

performed, considering any possible impacts, such as different materials for the car model in simulations like aluminum, plastic, rubber, and glass. Moreover, various scenarios are carried out in the simulation setup to take into account any possible point in VC, such as different antenna positions on the roof and inside of the car, more than one car and also one motorbike between them, and finally, obstacles between the vehicles and around them made of metal and bricks to see how the antennas perform in these situations.

To overcome the challenges and improve the recent related works, the proposed antenna utilizes a reliable technique by combining the leaky wave and SSPP structures fed parasitically and orthogonally logarithmic spiral-like strip resonators through two ports. By combining these two structures, the frequency-dependent nature of LWAs and SSPP is changed to improve the OBS issues of the LWAs and make them move towards the frequency-independent structure. In addition, this combination and the logarithmic spiral-like structure create multiple modes and more than one wide band, offering a stable and similar behavior throughout the working bandwidth.

The proposed antenna can be a reliable solution for VCs, operating across critical frequencies in the lower 5G band (3.4 GHz), X-band (10 GHz), higher 5G, and mm-wave communications (24 GHz, 55 GHz, 60 GHz, and 80 GHz). Its dual polarization enhances signal robustness, reduces interference, and boosts data throughput since several obstacles usually exist in the path of cars, pedestrians, and infrastructures. The compact, low-profile, and semi-flexible design ensures easy installation and integration without compromising aesthetics or aerodynamics and does not take too much of the car's area. It provides stable performance in dynamic environments with a maximum directive gain of 11.6 dBi in air and 14.56 dBi in vehicles. Logarithmic spiral-like resonators and SSPP-TL structures improve gain, isolation, and polarization across bands, enabling long-range communication and better obstacle penetration. In addition, the SAR analysis confirms safety compliance, ensuring reliability and acceptance for modern vehicular systems.

The proposed antenna is an efficient solution for vehicular communication, supporting V2V, V2P, and V2I interactions. Its multi-band capability, dual polarization, high gain, and compact structure address diverse requirements. For V2V, it ensures stable and interference-free links. In V2P, it provides broad coverage for reliable pedestrian connectivity, enhancing safety. For V2I, it enables long-range communication with infrastructure, aiding smart city and ITS development. These features position the antenna as a key enabler for improving connectivity, safety, and efficiency in modern vehicular networks.

The paper is organized as follows: Section 1 offers an in-depth overview of the challenges and methods associated with designing antennas for vehicular communication systems. Section 2 details the geometric arrangement of the proposed multi-band antenna and the design principles employed. Section 3 explores the antenna's characteristics and presents a parametric analysis. Section 4 then outlines the practical performance metrics of the antenna. Finally, Section 5 concludes the paper by summarizing the key findings of the study.

2. Design Configuration

This section outlines the antenna's design methodology and configuration. The proposed MIMO SSPP LWA is initially tailored to operate within targeted frequency ranges and is later integrated with periodic nested semi-circular strip resonator (NSCSR) elements. The radiation properties of the single-port setup are analyzed before transitioning to a dual-port structure. To enhance isolation, reflection coefficients, radiation efficiency, and gain while addressing surface waves, NSCSR cells and meander lines are employed as a neutralization mechanism. The SSPP framework minimizes back and end-fire radiation, enabling elevated and efficient broadside radiation. At each stage of development, current

and electric field distributions are thoroughly examined. Optimization studies are then performed, leveraging realistic vehicle models to replicate practical scenarios. Key parameters are fine-tuned based on initial estimates, and the design process is systematically detailed.

2.1. The Configurations of SSPP and Their Defining Principles

Figure 1 depicts the phases involved in the antenna design process, beginning with a single-port arrangement that later evolves into a two-port configuration. This design is then combined with neutralization networks to improve overall performance. The antenna utilizes a single layer of substrate with $\epsilon_r = 3.2$ and thickness of $h = 0.125$ mm (Rogers 4830). The substrate's conductor layer is copper, measuring $18\ \mu\text{m}$ thick. The proposed antenna features a unique feeding approach, combining two orthogonal semi-elliptical transmission lines and periodic SSPP structures. Additionally, it includes a wide slot ground with an embedded meander line functioning as a DGS to improve matching, gain, and radiation efficiency. Figures 1 and 2 display the front and rear perspectives of the prototypes, along with the different stages of their design. Further details on each design stage will be discussed in Section 2.2.

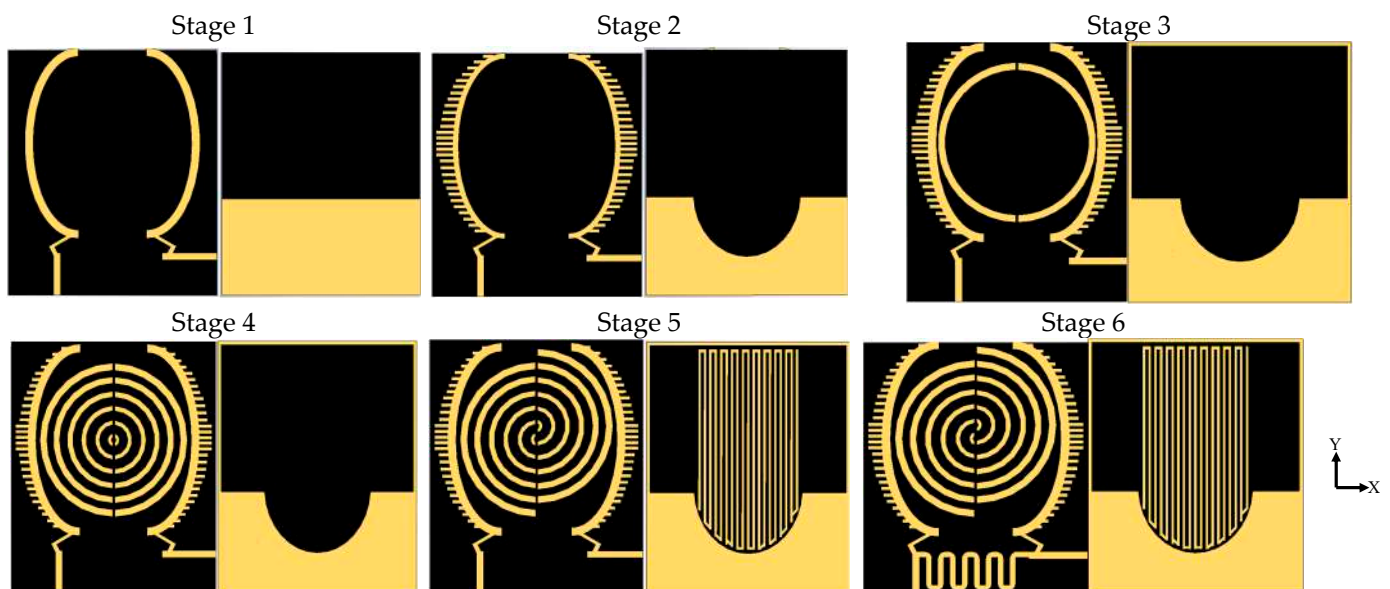


Figure 1. The design steps of the proposed antenna.

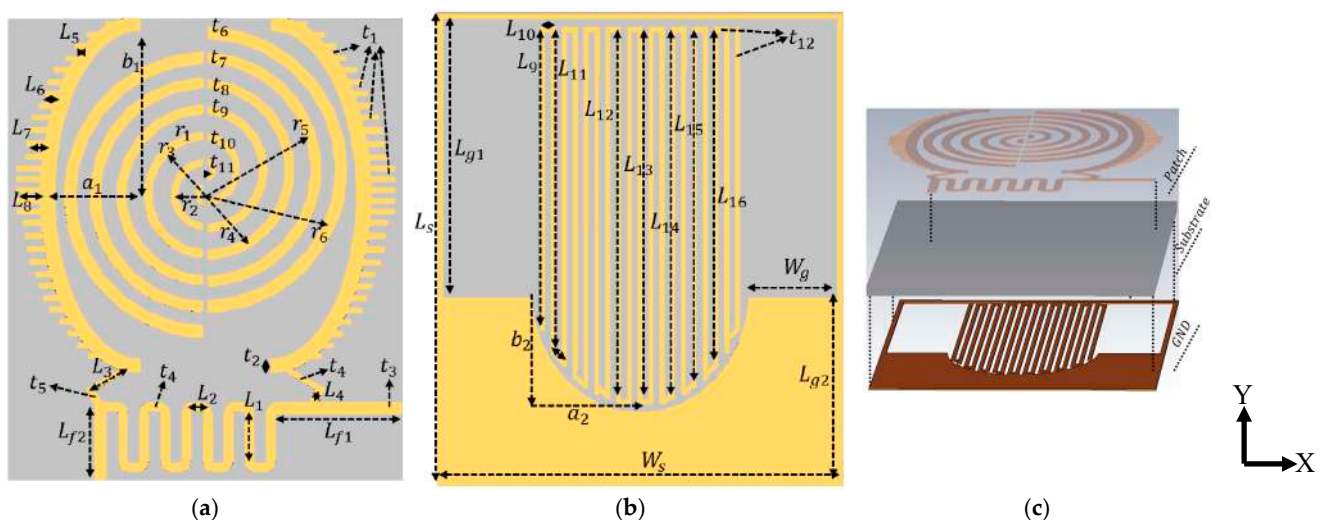


Figure 2. The design configuration (a): front view, (b): ground view, and (c): perspective view.

The proposed antenna is designed to be both compact and broadband, integrating semi-elliptical SSPP transmission lines (TLs) alongside parasitic NSCSR patches located on one side of the SSPP transmission line. This innovative design facilitates continuous beam scanning in both transverse and longitudinal directions through the utilization of two SSPP TL structures. The SSPP transmission line serves as a conductive pathway that supports a mode akin to surface plasmons, effectively emulating the surface wave behavior observed in subwavelength artificial structures. Notably, this SSPP mode remains non-radiative, confined to the interface between the conductor and the surrounding medium, and its high momentum results in a mismatch with conventional guided wave modes.

By employing two SSPP TLs, the single-conductor, low-loss configuration facilitates continuous beam scanning from forward to backward directions while ensuring efficient broadside radiation (using a single port). By tailoring the periodic structure of the SSPP waveguide, various modes (e.g., even, odd, or higher-order harmonics) can be supported at different frequencies, each corresponding to a specific radiation angle or pattern. Due to the periodic nature of SSPP structures and leaky wave principles, energy “leaks” into free space as the SSPP waves propagate, driven by periodic perturbations in the waveguide. The phase-matching condition between the guided SSPP mode and the radiated wave governs this leakage. Adjusting the periodicity allows different modes to radiate at varying angles. The SSPP modes transition into leaky modes when they reach specific cut-off frequencies or through intentional design modifications (e.g., tapering or impedance mismatching). Additionally, multiple leakage points enable multimode radiation over a broad frequency range. Furthermore, SSPP LWAs exhibit inherent frequency-dependent beam steering due to their dispersive properties. By exciting the antenna at different frequencies, each mode radiates in distinct directions or exhibits unique polarization characteristics. The small wavelengths at mm-wave and sub-THz frequencies make SSPP LWAs highly compact, making them ideal for integration into advanced systems such as 5G, 6G, or imaging technologies. SSPP structures can achieve wide bandwidths by optimizing their dispersion curves to support multiple modes over an extensive frequency range. This is crucial for applications requiring high-speed communication or high-resolution imaging.

The study delves into SSPP TLs’ resonance and transmission characteristics, the radiation mechanisms, and the overall performance of the antenna. Detailed analysis includes the dispersion curves of various cells of units and the SSPPs’ slow-wave characteristics. Additionally, SSPP structures contribute to improved matching and broadside radiation patterns, keeping the beams within a fast-wave region, as shown in Figure 3. According to Figure 1, the design process for the proposed antenna involves determining the dimensions of the monopole quadrangular patch and the SSPP (Single-Sided Parallel Plate) transmission line (TL) by employing fundamental equations from reference [33]. The objective is to construct an antenna with a length of half the wavelength, specifically measuring less than 18 mm at an operating frequency of 8.5 GHz. To achieve optimal performance, the ground length is designated as $\lambda_0/4$, which ensures a perfect impedance match and resonance at the designated frequency. The integration of the SSPP TL enhances the bandwidth and radiation patterns of the antenna, thereby facilitating effective beam steering. In the absence of the SSPP TL, the antenna may encounter limitations in efficiency and overall performance. For further information regarding conventional rig antennas, please consult reference [34].

$$W = \frac{c}{2f_0 \sqrt{\frac{(\epsilon_r + 1)}{2}}}, \quad \epsilon_{\text{eff}} = \frac{(\epsilon_r + 1)}{2} + \frac{(\epsilon_r - 1)}{2} \left(\sqrt{1 + 10 \left(\frac{h}{w} \right)} \right)^{-\frac{1}{2}}, \quad w = b - a \quad (1)$$

$$\Delta L = 0.412 h \frac{(\epsilon_{\text{eff}} + 0.3) \left(\frac{w}{h} + 0.264 \right)}{(\epsilon_{\text{eff}} - 0.258) \left(\frac{w}{h} + 0.8 \right)}, L_{\text{eff}} = \frac{C}{2f_0 \sqrt{\epsilon_{\text{eff}}}}, L = L_{\text{eff}} - 2\Delta L, L_g = L + (6h) \quad (2)$$

$$W_g = W + (6h), f_{\text{nm}} = \frac{X_{\text{nm}} \times C}{2\pi a \sqrt{\epsilon_r}}, a = \frac{F}{\left\{ 1 + \frac{2h}{\pi \epsilon_r F} \left[1.7726 + \ln \left(\frac{\pi F}{2h} \right) \right] \right\}^{1/2}} \quad (3)$$

$$F = (8.791 \times 10^9) / f_0 \sqrt{\epsilon_r}, a_e = a / \left\{ 1 + \frac{2h}{\pi \epsilon_r a} \left[1.7726 + \ln \left(\frac{\pi a}{2h} \right) \right] \right\}^{1/2} \quad (4)$$

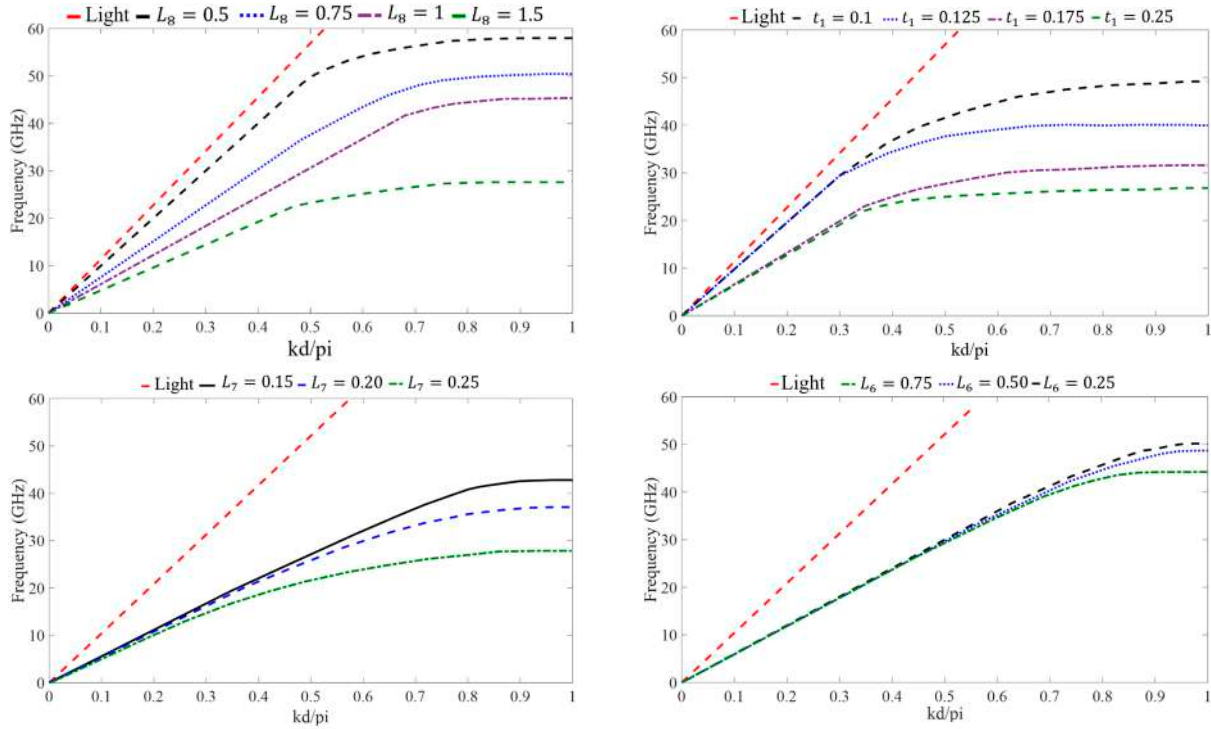


Figure 3. Variations of dispersion for the SSPP structures.

Here, the patch's width is represented by W , the speed of light is denoted by c , the resonance frequency is shown by f_0 , ϵ_r stands for the substrate's relative permittivity, the effective dielectric constant is ϵ_{eff} , L is the angular length of the patch, the extension length is denoted by ΔL , the effective length is signified by L_{eff} , the substrate thickness is denoted by h , the ground length is denoted by L_g , ground width is denoted by W_g , 'a' and 'b' are the inner and outer radii of the ring, w is the space between the rings, W_g is the width of the ground, X_{nm} is the first-order Bessel function root, depending on the mode of the patch, F is the resonating frequency, and a_e is the effective inner radii. In the above equations, we can obtain $X_{\text{nm}} = 0.6773$ for TM_{11} , $X_{\text{nm}} = K_{\text{nm}} \times a$, $\frac{b-a}{b+a} < 0.35$, and $b = 2a$. Port 2 is configured to receive signals perpendicularly in order to facilitate dual polarization. A semi-elliptical slot is etched from the layer of ground to effectively minimize fringing fields, thereby enhancing the bandwidth at resonant frequencies and improving the performance of radiation modes.

The next step is to apply the proposed SSPP structures to the transmission lines. The design of the periodic cells affects how the SSPP mode behaves. When the SSPP scaling factors (called P_1) or the stub lengths (L_{5-8}) are increased, the frequency of the SSPP mode decreases. The stub width (t_1) and the gap between the periodic units also affect how the SSPP mode transmits. This effect is shown in Figure 3. The fast-wave region is on the left side of the light line, while the slow-wave region is on the right. Figure 3 illustrates that the dispersion curves for the SSPP transmission line, with different stub lengths (L_{5-8}),

gradually move away from the light line. Longer SSPPs (L_{5-8}) lead to better confinement and a lower cut-off frequency.

In the LWA, the SSPP transmission line (TL) functions as the feeding structure, where electromagnetic waves are tightly confined to the TL in transmission mode. Periodic rectangular metallic strips are used to modulate the transmission line, thereby inducing the unbounded radiation mode. Due to the periodic nature of these structures, multiple spatial harmonics are generated in accordance with Floquet theory, with the phase constants expressed as follows:

$$\beta_n = \beta_0 + \frac{2n\pi}{p}, n = 0, \pm 1, \pm 2 \dots \quad (5)$$

where β_n is the phase constant of the n th-order space harmonics, β_0 is the phase constant of the fundamental transmission mode, and p is the modulation periodicity. It can be seen that to get a fast wave of space harmonics, it should be $n < 0$. The $n = -1$ space harmonic is usually chosen. Herein, the phase constant of the -1 st order harmonic is given by $\beta_{-1} = \beta_0 - (2\pi/p)$. Consequently, the primary beam direction of the LWA is determined using the formula $\theta = \arcsin(\beta_{-1}/K_0)$, where K_0 represents the wavenumber in free space [35,36].

It is important to highlight that the Eigenmode Solver in Computer Simulation Technology (CST) Microwave Studio, an electromagnetic simulation software, is used to calculate the dispersion curve of the unit cell. The boundary conditions must be set meticulously in accordance with CST's guidelines: $E_t = 0$ should be applied for the boundaries at X_{min} - X_{max} and Y_{min} - Y_{max} , while Z_{min} - Z_{max} must be defined as periodic. A "phase" parameter is then assigned to the periodic boundary to facilitate a parameter sweep for analyzing the frequency dispersion characteristics of the proposed SSPP structure. A user-defined watch template can be customized to include additional watches. The parameter sweep watch encompasses group velocity, phase velocity, and dispersion plots for the first mode, all available in the '1D Results' folder of the navigation tree. Results for power flow and Pierce Impedance are also found in this folder. To view or modify the parameter sweep source code, engage the "Edit" option in the parameter sweep window (for further details, refer to CST's help documentation).

Figure 4 illustrates three separate frequency zones. The antenna functions within the fast-wave region, spanning from 3 GHz to 24 GHz, distinct from the airline represented by the dashed black line. Broadside radiation occurs at frequencies of 8.5 GHz, 18 GHz, 28 GHz, and 45 GHz. Moreover, backward radiation is observed between 10 GHz and 22 GHz, while forward radiation is evident from 22 GHz to 42 GHz. An example design is presented for broadside radiation. By applying Equation (1) and associated formulas, it is determined that β_0 equals $2\pi/p$, with β_0 being derived from k in Figure 3. Initially, the periodicity p is roughly 0.32 mm near 18 GHz, but after refinement, it is confirmed at 0.30 mm.

After the transmission wave couples from the SSPP (TL) to the semi-circular strip patches, it emits as a space wave [37]. As illustrated in Figure 5, strong coupling and high leakage efficiency occur as the wave traverses all patches. Creating a consistent phase plane is critical for maximizing gain in spatial radiation. The gap between the strips significantly influences the in-phase surface and the working frequency. To clarify the frequency characteristics of the proposed dual-port antenna, the electric field component E_z distributions on the XoY plane, positioned approximately 1 mm above the substrate, are shown at various frequencies in Figures 5 and 6. Within a range of less than 10 GHz, the electric field E_z gradually diminishes from one port to another, signifying continuous electromagnetic radiation into free space. The mode fields in the SSPP transmission line are primarily concentrated in the deeper sections. At frequencies exceeding 10 GHz, the electric

field weakens since the majority of the energy has already been emitted. Nevertheless, at 18 GHz and above, significant electric field concentrations are observed in both the SSPP transition area and the antenna element section, demonstrating that the electric field energy is effectively transmitted between the two ports.

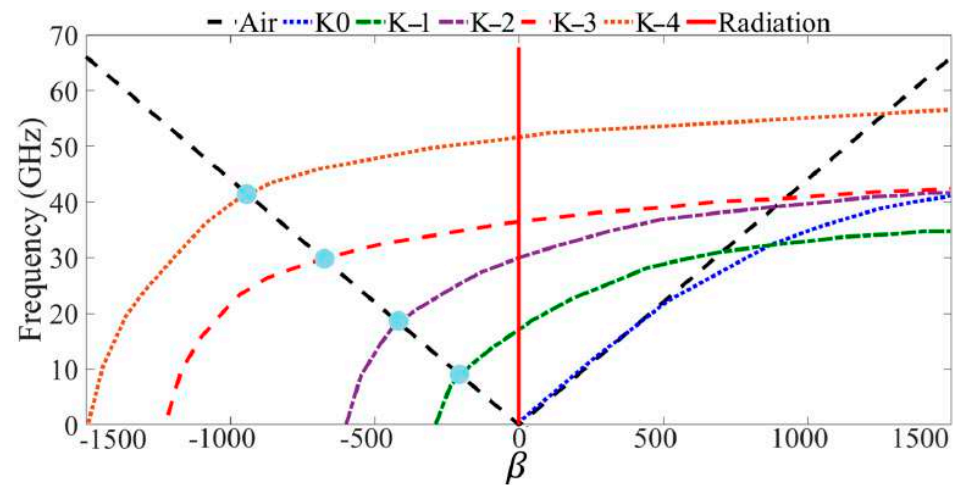


Figure 4. The dispersion curves of SSPP unit cell.

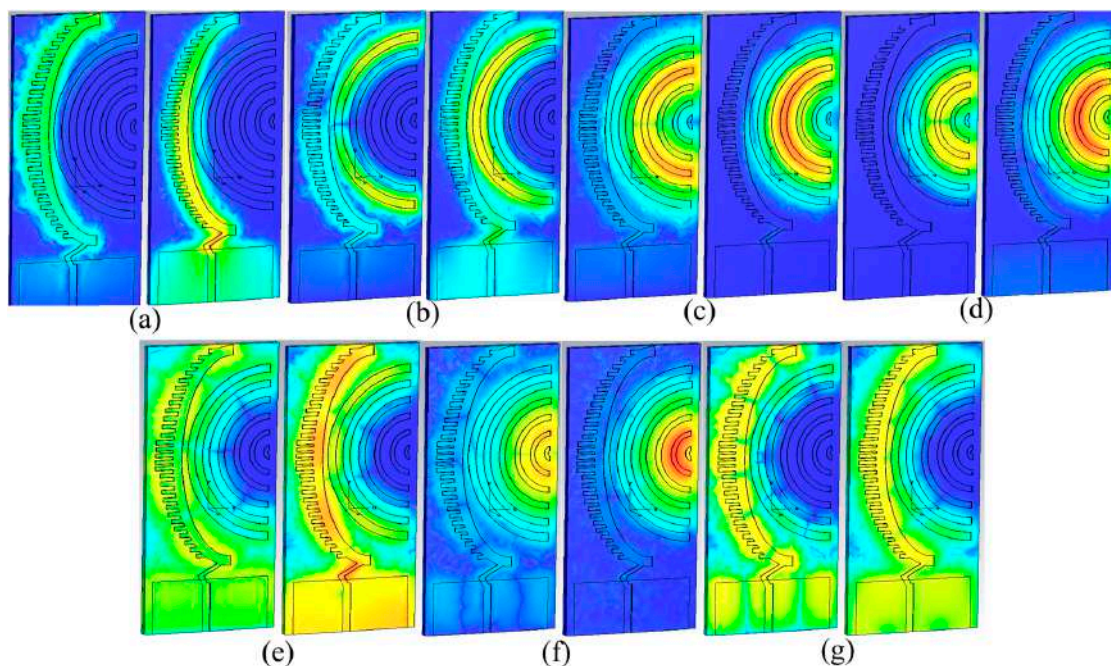


Figure 5. Computed distributions of the E and H fields for the suggested one-port SSP LWA are shown at the following frequencies: (a) 3.4 GHz, (b) 8.5 GHz, (c) 18 GHz, (d) 24 GHz, (e) 35 GHz, (f) 60 GHz, and (g) 80 GHz (The red and blue colors are the minimum and maximum, respectively).

The single-port antenna facilitates lateral radiation with a single-beam scanning capability, achieved through its asymmetric modulation along the transverse axis. This design effectively mitigates the typical issue of dual beams, which often arises due to the absence of a ground plane in the SSPP transmission structure. The approach incorporates periodic semi-circular strip loading along the +X side of the SSPP transmission line. By carefully adjusting the dimensions of these strips, a phase shift is induced in opposing directions, ensuring the electromagnetic fields remain in phase along the +X and +Y axes while becoming out-of-phase along the −X and −Y axes. As a result, the majority of the energy radiates toward the +X and +Y directions, with reduced emission toward the −X and −Y

directions. When an additional feed is placed orthogonally, the antenna supports both sideward and longitudinal radiation. Figure 7 displays the phase distribution of the SSPP LWA at different frequencies, highlighting strong radiation behavior in both forward and backward directions.

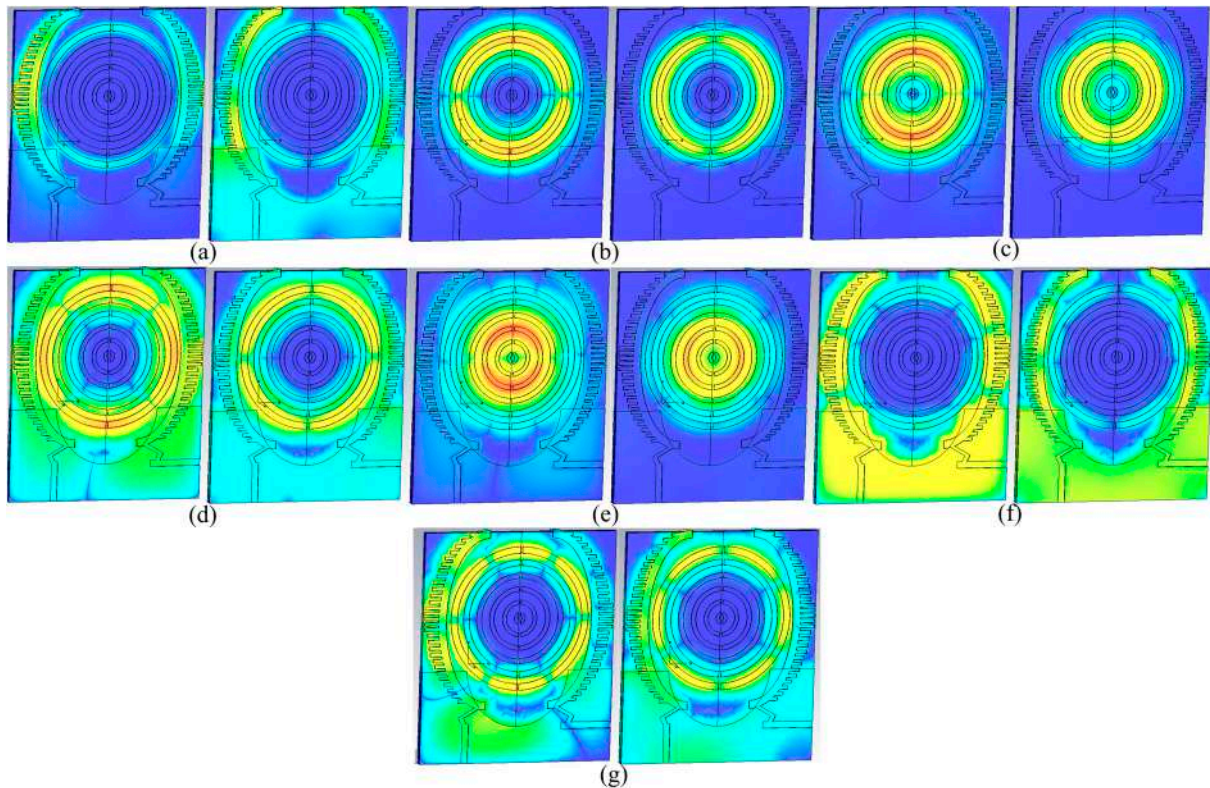


Figure 6. Modeled patterns of the E/H fields for the two-port designed antenna at the following frequencies: (a) 3.4 GHz, (b) 8.5 GHz, (c) 18 GHz, (d) 24 GHz, (e) 35 GHz, (f) 60 GHz, and (g) 80 GHz (The red and blue colors are the minimum and maximum, respectively).

2.2. Leaky Wave Designs, Their Fundamental Concepts, and Integration with SSPPs Section

The development of the proposed LWA follows established guidelines, formulas, and industry standards critical for such antennas. A key concept is that the resonant frequency is significantly influenced by variations in the antenna's length. Typically, there is an inverse correlation between the antenna length and its resonant frequency: increasing the length lowers the resonant frequency, whereas decreasing it raises the frequency. This dependency arises from the core principles of electromagnetic wave propagation and the antenna's structural characteristics.

The design of the leaky-wave structure emphasizes achieving high performance in terms of directivity, gain, low losses, and structural simplicity. As a member of the traveling-wave antenna category, LWAs operate by guiding waves along structures longer than their wavelength. This wave motion generates longitudinal currents, producing end-fire and back-fire radiation patterns influenced by the open-stopband (OSB) effect, as referenced in [38,39]. These antennas are typically represented by a balanced composite right-/left-handed (CRLH) transmission line model, accounting for the roles of inductors and capacitors. Nevertheless, adjustments are necessary to facilitate radiation in the broadside direction from both the antenna and the vehicle.

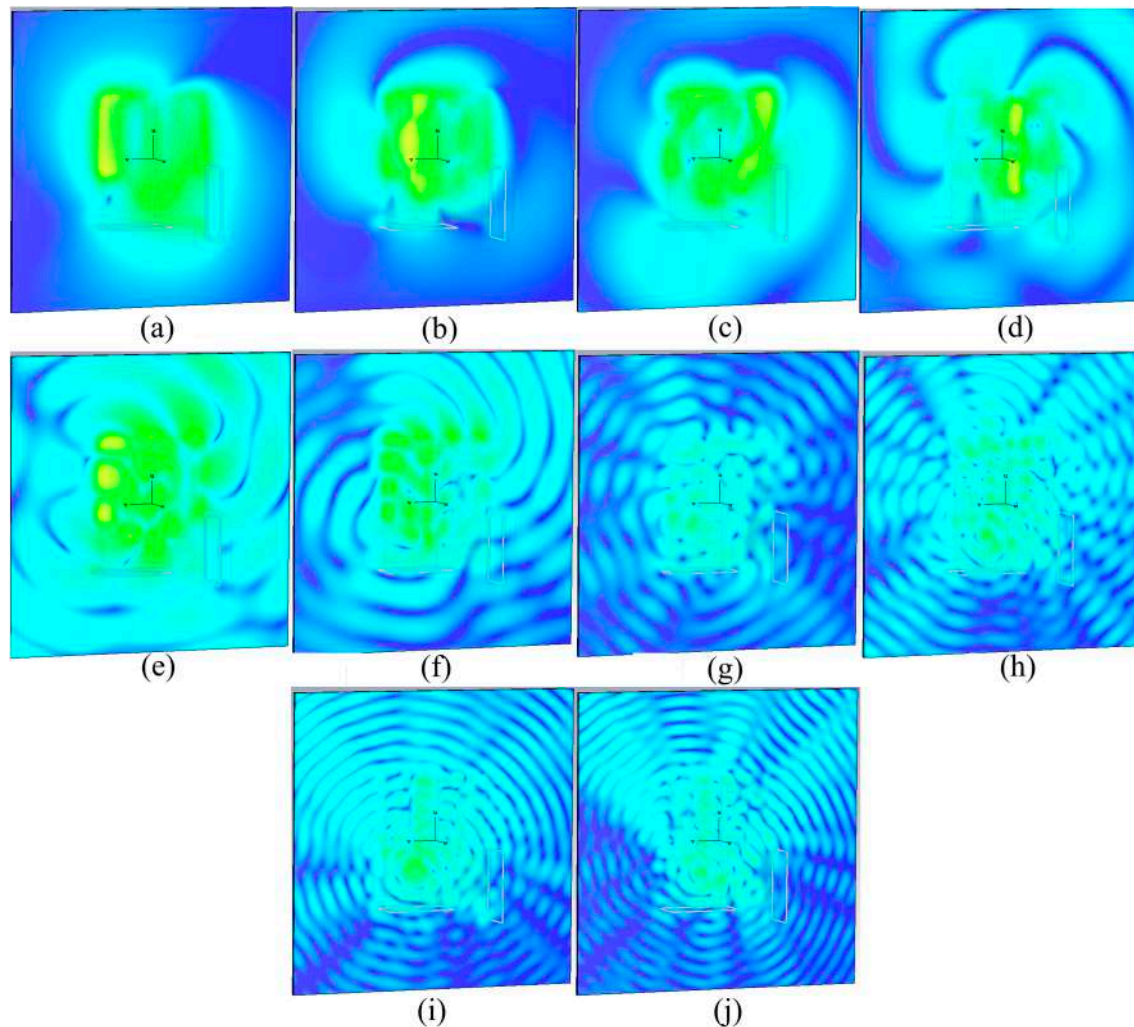


Figure 7. The proposed antenna's phase distribution at (a): 3.4 GHz, (b): 5.6 GHz, (c): 10 GHz, (d): 18 GHz, (e): 24 GHz, (f): 28 GHz, (g): 35 GHz, (h): 50 GHz, (i): 60 GHz, and (j): 80 GHz (The yellow and dark blue are the maximum and minimum, respectively).

To understand the antenna's design process, it is essential first to comprehend the fundamental principles of LWAs and how slots and stubs influence key parameters like impedance bandwidth and radiation patterns. The proposed SSPP LWA incorporates asymmetrical features, such as longitudinal stubs to enhance OSB suppression and transverse stubs to address OSB-related issues. These stubs function similarly to left-handed capacitances (CLs), shaping the radiation pattern to prioritize broadside emission over end-fire or back-fire directions. Moreover, the stubs help to minimize surface waves commonly generated by LWAs. The characteristic mode approach is employed to design and evaluate the slots, focusing on their effect on the radiation pattern and achieving asymmetric radiation [40]. In this design, the waveguide port must excite the TE_{10} mode rather than the TE_{01} mode typically associated with dielectric insets. This approach leverages an asymmetrical structure to improve OSB suppression, aligning the radiation mechanism with the structural asymmetry. When the periodic strips are symmetrically positioned relative to the sidewalls, the vertically polarized TE_{10} mode fails to produce a horizontal field in the antenna aperture. This principle governs the transverse sections of the periodic stubs, ensuring that the emitted electromagnetic waves are polarized orthogonally to the antenna's longitudinal planes. The TE_{10} mode, which is horizontally polarized, is excited through the dielectric inset, allowing the radiation to rely solely on this mode and

negating the need for asymmetry to induce radiation. Additionally, by adjusting the gap between stubs, it is possible to regulate the inset's leakage rate, offering further control over the antenna's performance. This configuration utilizes a blend of periodic protrusions (patches) and two distinct periodic SSPP designs to regulate the leakage rate by altering the asymmetry of gaps, particularly by adjusting the spacing between elements of the SSPP structures, as outlined in the SSPP segment.

Following the evaluation of SSPP and leaky-wave structure concepts, an extra leaky-wave array featuring periodic semi-circular strip elements and a second port was incorporated. This adjustment enhances the bandwidth at the initial two radiation modes (approximately 3.35 GHz and 24 GHz) and introduces an additional wideband near 33 GHz. Furthermore, the gain and radiation efficiency see improvements throughout the operational frequency range. Although the integration of the leaky-wave and SSPP structures delivers high gains and broad bandwidth, the antenna's radiation remains bidirectional and end-fire-oriented due to the imperfect ground plane. To resolve this issue, meander lines were implemented along with the defective ground to reduce radiation leakage and direct the antenna's radiation toward the broadside direction (stage 4). Furthermore, pairs of semi-circle strips were added based on their respective resonances to boost gain and radiation efficiency by increasing surface wave activity in that region. The size and spacing of these strips were optimized according to the surface current distribution (SCD) and E/H fields observed around them, as shown in Figures 5 and 6. This adjustment also broadens the working bandwidth around the third and fourth radiation modes, extending it to cover the bands of 32–41 GHz, 55 GHz, and 75–81 GHz (stage 5). Once the required radiation modes and operational bands were achieved, the second set of semi-circle arrays were shifted towards the +Y direction to create a spiral-like structure. This enhances the antenna's circular polarization capabilities, reduces OSB, and improves its multi-resonance and multimode functionalities. Lastly, a chamfered-edge meander line neutralization network was developed to enhance port isolation (stage 6). The meandered structure further supports the antenna's multi-frequency characteristics. Table 2 outlines the dimensions and refined parameters for the different elements of the proposed antenna. These values were initially calculated using relevant formulas and subsequently adjusted through parametric analysis to achieve optimal performance.

Table 2. The proposed antenna's structural parameters.

Parameters	Values (mm)	Parameters	Values (mm)	Parameters	Values (mm)	Parameters	Values (mm)
L_s	14	L_{10}	0.50	t_2	0.55	r_4	3.12
L_{f1}	3.15	L_{11}	9.00	t_3	0.50	r_5	4.12
L_{f2}	2.5	L_{12}	12.75	t_4	0.25	r_6	5.12
L_{g1}	7.20	L_{13}	13.25	t_5	0.30	L_9	8.25
L_{g2}	6.80	L_{14}	13.25	t_6	0.5	t_1	0.25
L_1	2.85	L_{15}	10.75	t_7	0.45	r_3	2.12
L_2	1.10	L_{16}	10.75	t_8	0.40	L_8	0.90
L_3	1.40	W_s	12.00	t_9	0.35	b_2	3.80
L_4	0.65	W_g	3.25	t_{10}	0.30	r_2	1.12
L_5	0.45	a_1	3.60	t_{11}	0.25	L_7	0.75
L_6	0.60	a_2	3.80	t_{12}	0.20	b_1	4.85
r_1	0.12						

Based on the evaluation of the proposed design and the design stages shown in Figure 1, the SCD for each step of the antenna development is displayed in Figure 8. In this figure, it is evident that the current density of the antenna is most concentrated at stage one of the design near the transmission line when port 1 is activated. At stage two, corresponding to the first mode at 3.4 GHz, the SCD reaches its peak intensity around the

transmission line and the periodic SSPP structure. In phase 3, a significant current flows along the SSPP structures, influencing the first two large semi-circular strips (corresponding to the second mode at 10 GHz). It also demonstrates that the surface current distribution (SCD) near the SSPP-TL, along with the inclusion of another semi-circular strip, plays a crucial role, as depicted in phase 4 (third mode at 27 GHz). A similar pattern is observed in phases 5 and 6, where a higher current density is concentrated around the newly added, smaller strips (associated with the fourth mode at 55 GHz and 80 GHz) and the meander-line neutralization network. Furthermore, it highlights that with the addition of these strips and the meander lines, no current flows near the second port, ensuring port two is completely isolated.

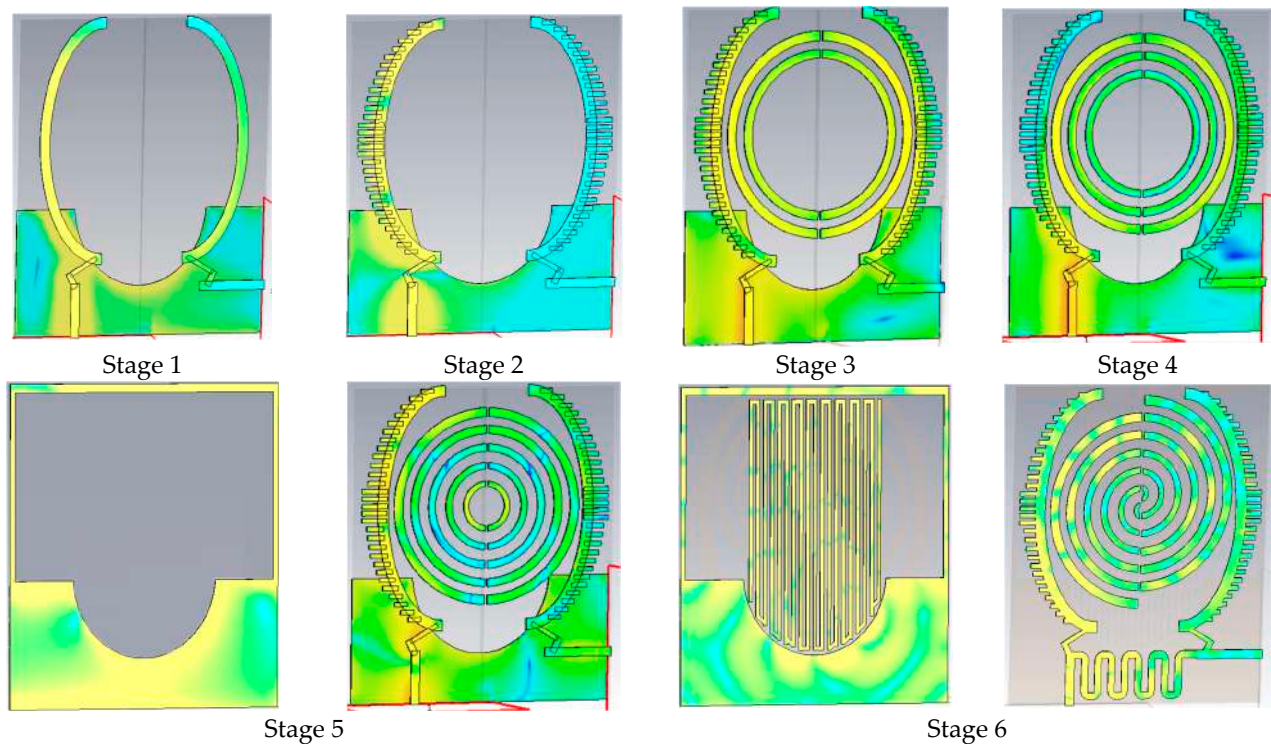


Figure 8. The SCD of the proposed antenna across stages 1 through 6 (The red and blue colors are the maximum and minimum, respectively).

The antenna can be fine-tuned and enhanced via a parametric analysis, during which five key parameters that significantly impact the initial design are modified. Figure 9 presents adjustments to various parameters, including the semi-elliptical ground slot dimensions (a_2 , b_2), SSPP section lengths (L_5 – L_8), wide ground slot length (L_{g1}), feed line measurements (L_{f1} , L_{f2}), and semi-elliptical transmission line (TL) dimensions (a_1 , b_1). When the minor radius of the semi-elliptical TL is reduced to less than 3.5 mm, only higher-band harmonics are observed, with frequencies below 22 GHz completely eliminated. Conversely, increasing the minor radius to 5.5 mm alters the behavior significantly, introducing lower-band harmonics below 10 GHz alongside additional higher resonances. A comparable effect is seen with the major radius (b_1), where expanding it to 4 mm causes a slight shift in frequencies below 8 GHz, leading to a decline in performance for the second and fourth radiation modes. Figure 9b demonstrates the variation in the reflection coefficient regarding the semi-elliptical slot's dimensions on the ground. It shows that when the minor and major radii of the antenna are less than 2 mm, the first three modes of radiation are obtained with narrower BW, but the fourth modes of radiation are degraded and not working. However, when the minor and major radii of the TL are increased

and reach 4.5 mm, all the resonance and radiation modes are achieved with wider BW at the lower and middle band of the frequency.

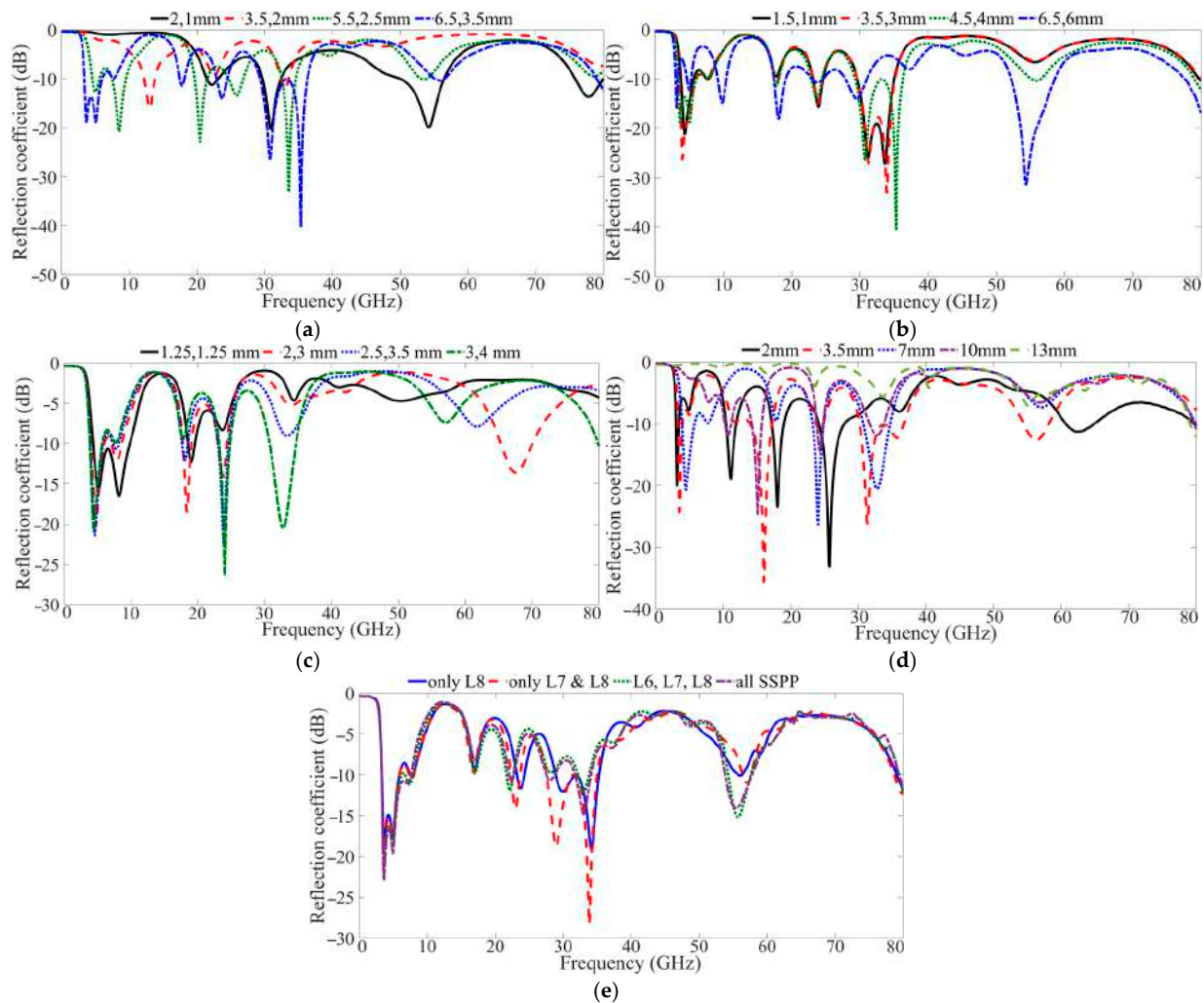


Figure 9. A parametric study of five essential parameters in terms of reflection coefficient results in (a): a_1, b_1 ; (b): a_2, b_2 ; (c): L_{f1}, L_{f2} ; (d): L_{g1} ; and (e): SSPP array.

Figure 9c depicts that for the 3–3.5 mm feed line length, almost all the radiation modes are created with wider BW for the lower bands for the lower 5G communications. The reflection coefficient variation of the antenna in terms of the length of the wide slot in the ground layer is illustrated in Figure 9d, which shows that the antenna has the best performance and matches the working band when the length is 5–7 mm. It also depicts that exceeding it degrades the radiation's first and last mode of the radiation. The impedance BW of the antenna in terms of the SSPP arrays is shown in Figure 9e. The positive impacts of the periodic SSPP arrays are evident in the working bands for each associated resonance and the radiation modes and in improving the BW for each mode.

A reflection coefficient behaving similarly across a broad frequency range (from DC to 80 GHz) is often due to specific design characteristics of the system or device under test. Since the proposed antenna is designed for multi-wideband impedance matching, its reflection coefficient remains relatively low across a broad frequency range. This ensures minimal reflections, leading to uniform behavior. Furthermore, patch structures as logarithmic spiral antennas are frequency-independent designs that inherently maintain consistent impedance characteristics over the working frequency range. In addition to the logarithmic spiral structure of the patch-producing frequency-independent structure, the

proposed antenna uses more than one operating mode and multiple periodic SSPP structures, each affecting different working frequency ranges, to create an aggregate behavior that appears frequency-independent. Moreover, the combination of the leaky wave and the SSPP structures also improves those characteristics [41].

Following the parametric analysis of the proposed antenna, the S-parameter results for the MIMO antenna are shown in Figure 10. It should be mentioned that these variables are optimized, and their results are shown in Figure 10 for the reflection coefficient (a), the transmission coefficient (b) for each step of the design, and the final S-parameter results for two port MIMO antenna. It shows that the associated bands for each design stage are achieved at the related bands. For instance, the resonances around 3.4 GHz and 24 GHz are obtained at stage 1. At stage 2, the third mode of radiation and resonance gets around 35 GHz, keeping the first two bands and increasing the working BW. Moving forward to the third, fourth, and up to the 6th stages, the other bands also achieved and kept improving the BW. Furthermore, adding the meander lines, the DGS, and the naturalization network improved the level of transmission coefficient and the isolation from -5 dB up to -20 dB. The final S-parameters results of the two port MIMO antenna are also presented in Figure 10c to understand the antenna's capabilities and impedance matching at the desired bands.

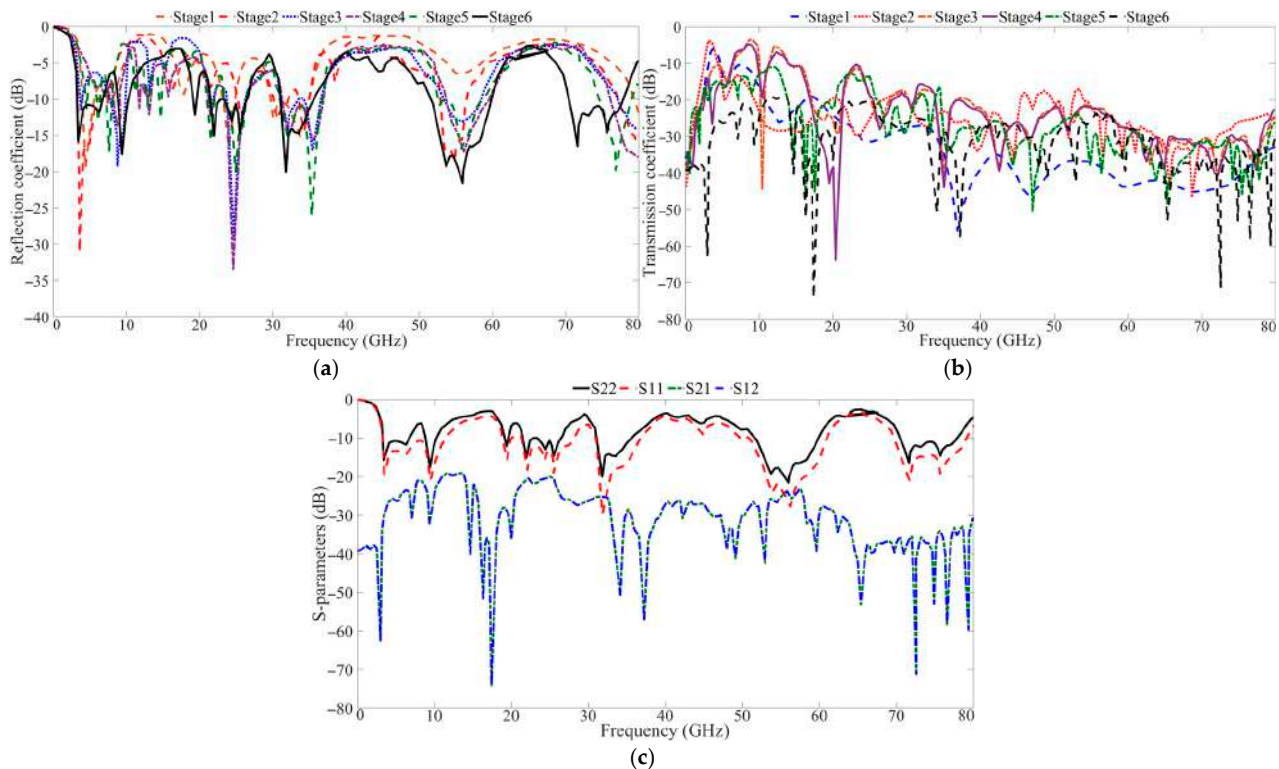


Figure 10. The S-parameter results of the proposed MIMO after parametric study (a): reflection coefficient, (b): transmission coefficient, and (c): two-port MIMO results.

Another important consideration is the beam steering capability and scanning range of the proposed antenna. Key parameters influencing beam steering performance, including scanning range, scanning rate, and beam coverage, are subsequently evaluated. Considering the limited bandwidth of LWAs, the concept of scanning rate (S) can be extended to an average scenario. It is defined as the ratio of the scanning angle range to the antenna bandwidth, as expressed by the following equation $S_{\text{average}} = \Delta\theta / \Delta f = (\theta_2 - \theta_1) / (f_2 - f_1)$. Here, θ_1 and θ_2 are the starting and ending angles of the scanning range. f_1 and f_2 correspond to the working frequencies of θ_1 and θ_2 . However, it is important to notice that the

average scanning rate in the last equation only considers the absolute bandwidth. However, relative bandwidth is more important in evaluating their spectrum efficiency for normal electronic systems. So, it is reasonable to replace the absolute bandwidth Δf in it with the relative bandwidth $\Delta f/f_c$, $S_{RASR} = \Delta\theta/(\Delta f/f_c)$ [42]. Here, S_{RASR} refers to the relative average scanning rate, while f_c represents the central operating frequency. Once these parameters are computed for each operational band of the designed antenna, their final values are summarized in Table 3.

Table 3. Coverage parameters of the proposed LWA.

Frequency Bands (GHz)	Scanning Range/Beam Coverage (°)	Scanning Rate (°/GHz)	SRASR (°)
3.32–4.28	172–180	8.33	333.4
8.45–11.7	4–167	50.15	2007.4
16.66–18.45	13–127	63.69	2547.5
23.67–27.26	47–150	28.7	1147.8
31.67–34.57	34.57–31.67	33.8	1351.7
52.3–61.67	53–11	4.48	179.4
71.8–82.5	11–48	3.45	138.3

To illustrate the isolation and performance of the antenna more clearly, the radiation pattern overlap of the antenna at the working bands is presented in Figure 11 and Table 4. These visualizations from Figure 11 and Table 4 show the spatial distribution of radiated power from each port and confirm that the overlap between patterns is minimal, even at the higher frequency bands. This confirms the claim of achieving excellent port isolation. The 2D far-field radiation patterns/polar are plotted to depict the radiation from each port and also to show how minimal they overlaid. Table 4 presents the half-power beam width (HPBW) and the main lobe of ports 1 and 2's radiation pattern in detail at different frequencies. Table 4 also shows that the radiation is well separated, much more than the minimum acceptable angle.

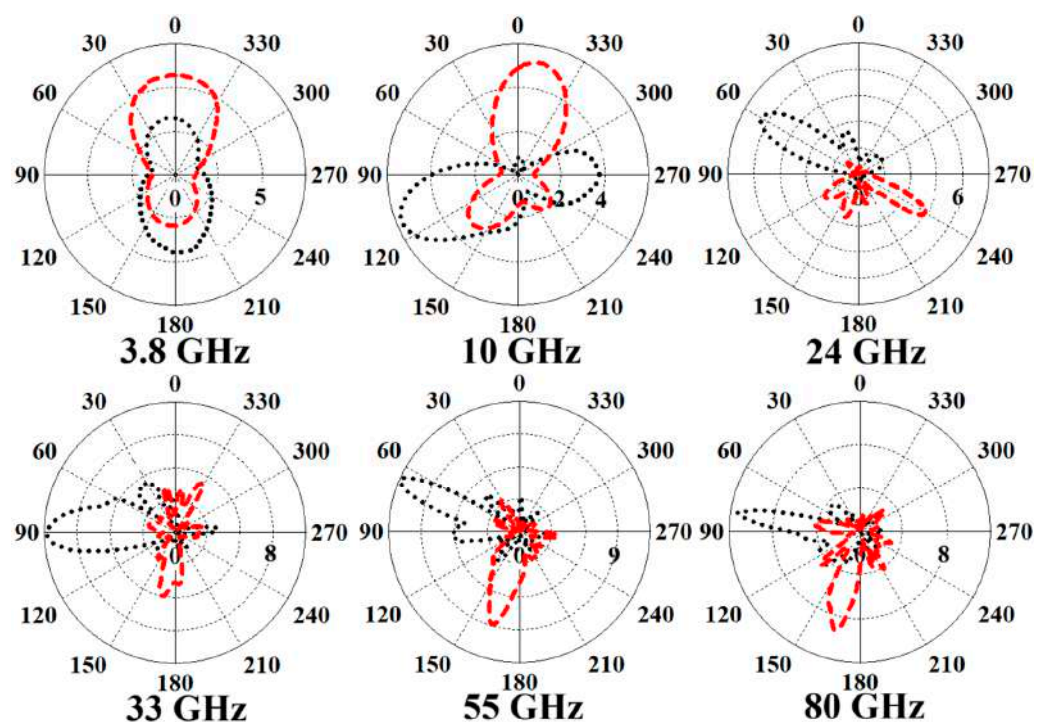


Figure 11. Radiation patterns overlap between ports 1 and 2: black dotted line is port 1, red dashed line is port 2.

Table 4. The radiation pattern overlaps between ports 1 and 2 in detail.

f_r (GHz)		3.8	10	24	33	55	80
HPBW (°)	P ₁	68	73	32	29	20	18
	P ₂	69	74	32	31	23	26
Main lobe direction (°)	P ₁	175	112	60	91	66	82
	P ₂	1	349	238	169	164	166

3. Evaluation of the Antenna's Performance in a Vehicular Environment

The initial step involves identifying the best placement on the vehicle to maximize radiation toward the desired directions for the proposed antenna. For our simulations, we utilized a Volvo car model (V90, the estate version of the S90) sourced from [43], as well as a Porsche model (911 Turbo) and a basic bike model obtained from [44]. The primary structure was modeled as a perfect electrical conductor (PEC), while other components represented standard vehicle materials such as polymers and aluminum. Typically, horizontal coverage is crucial for V2V and V2P communication, with a zero-elevation angle being adequate. However, V2I and V2N communications need a higher elevation angle. Thus, for V2X communication, the mm-wave antenna should be designed for horizontal and vertical transmission (supporting dual and circular polarization). Mounting the antenna at an elevated position, such as on the vehicle's roof, effectively reduces interference from nearby cars, buildings, dense foliage, or bridge pillars. This approach minimizes obstructions and supports line-of-sight communication [45]. Additionally, placing the antenna on the roof allows more flexibility for alignment compared to the bumper, which limits radiation to the front and rear.

The proposed antenna needs high gain to compensate for substantial path loss, in addition to dual and circular polarization that further enhances performance. To determine the effectiveness of the compact MIMO SSPP LWA antenna for vehicular communication, we used CST Studio Suite software to analyze its performance on the car's rooftop, evaluating metrics such as impedance matching, gain, radiation efficiency, and directivity. As shown in Figure 12, the antenna is placed at the front and rear edges of the rooftop, on all four sides, and when two cars and a bike are present between them. Figure 13 illustrates the impact of the car's metallic body (different materials are considered for all the vehicles, such as steel, aluminum, rubber, polymer, and fiberglass) and PEC on the antenna, showing slight impedance bandwidth mismatches, a frequency shift, and an increase in gain. For example, with the antenna at the front, we achieve a reflection coefficient of <-9.23 dB in the working bands (3.2–8.5 GHz, 24–26 GHz, and others), a maximum gain of 11.85 dBi, and a peak efficiency of 89%. With antennas positioned at both the front and rear, we observe a maximum gain of 14.5 dBi and an efficiency of 92.31%. This trend is consistent across the placements in Figure 12, with bandwidth, gain, and efficiency improvements when the antenna is mounted on the vehicle rather than in free air. Due to the significant path loss associated with 5G millimeter-wave frequencies, this high-gain antenna configuration is perfectly suited for short-distance communications, including V2V and V2I applications [46]. Figure 13 also demonstrates strong isolation with minimal coupling on the rooftop, both front-to-back and in configurations with multiple antennas, including scenarios involving two cars and a bike. The SSPP LWA design, shown in Figure 13, offers effective beam alignment for wide horizontal coverage without excessive cost and complexity, fulfilling the requirements for V2X communication. Furthermore, Figure 13 confirms excellent port isolation in each configuration (>25 dB across most bands and >20 dB at some lower bands).

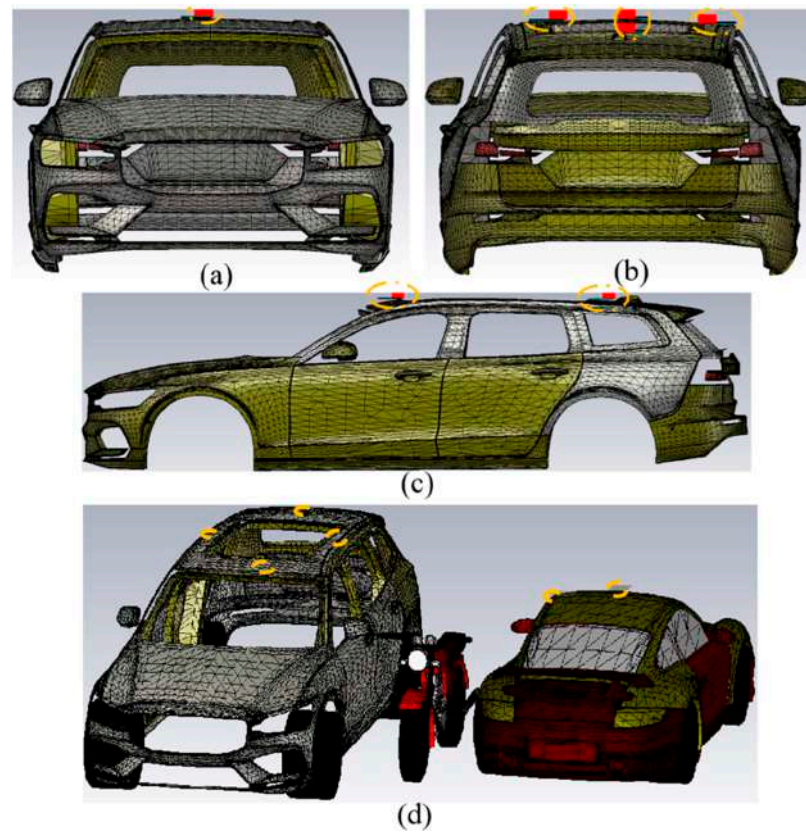


Figure 12. Evaluations for automotive scenarios using the suggested antenna positioned on the roof (a) front, (b) four sides, (c) front and back, and (d) on two cars when one bike is between them.

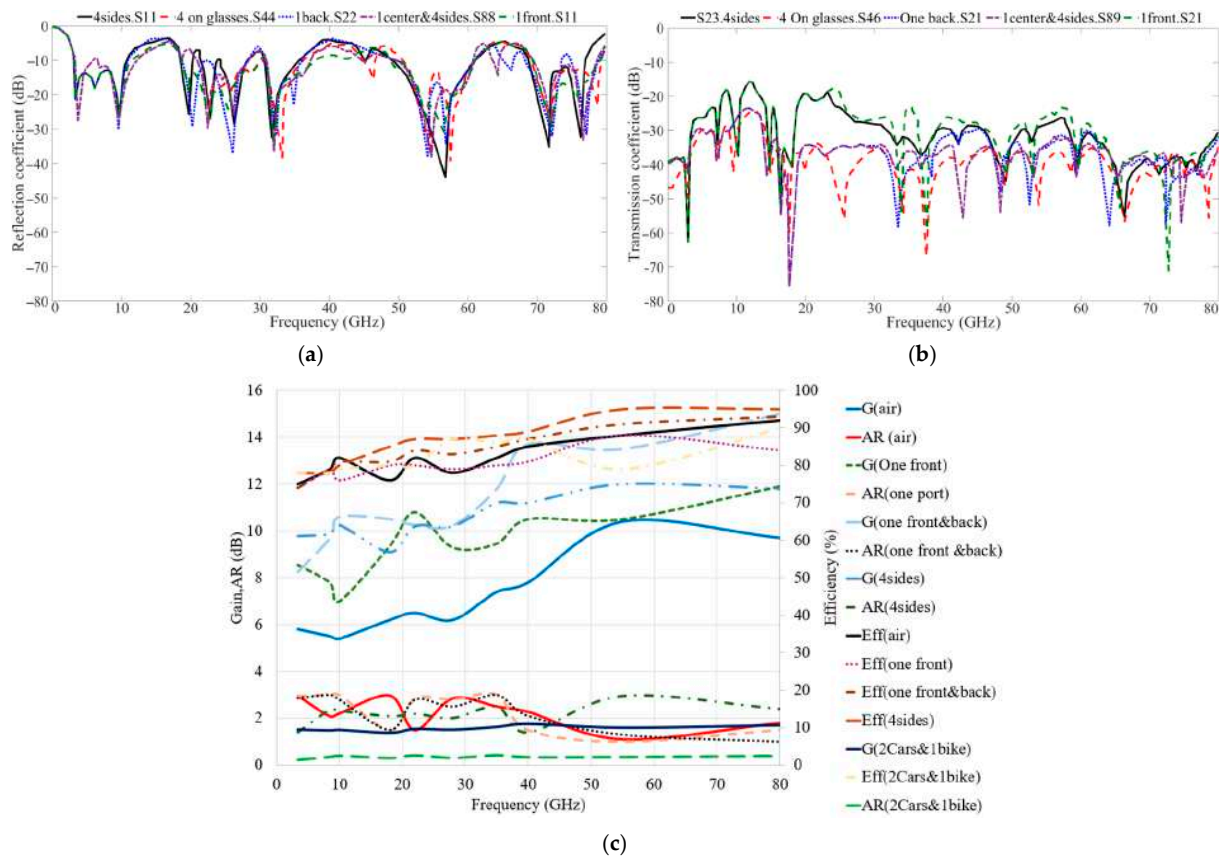


Figure 13. Effect of the vehicle body on the proposed SSPP LWA: (a) reflection coefficient, (b) transmission coefficient, and (c) gain, AR, and radiation efficiency.

To consider more realistic scenarios in our assessment of antenna capabilities for communication and show the antenna can work reliably, two more simulation setups are carried out, such as considering two more antenna arrays inside the car to evaluate the in-vehicle communication and when more obstacles (between two cars, walls surrounding the car, and also soil beneath the cars) with different materials like metal and bricks are utilized.

The other scenario is considering several obstacles with different materials. In such an environment with metallic and brick poles as obstacles, walls next to the cars, and solid ground beneath them, the reflection coefficients (S_{11}), transmission coefficients (S_{21}), and radiation patterns are affected (Figure 14). As it was shown in Figure 14, the reflection coefficient level is slightly degraded due to reactive coupling and impedance mismatch caused by nearby reflective surfaces such as metallic poles, walls, and the ground as compared to the other scenarios. For instance, more stopbands. These obstacles also shifted the resonance frequencies and narrowed the impedance bandwidth, particularly at lower frequencies where longer wavelengths interact strongly with larger objects. On the other hand, the transmission coefficients are also influenced by the multipath environment, as obstacles and walls introduce scattering, diffraction, and attenuation, especially in millimeter-wave (mm-wave) bands where line-of-sight (LOS) communication is critical. The presence of walls and ground reflections creates multipath interference, leading to signal fading or enhancement depending on the constructive or destructive overlap of paths. However, the effects are not dramatic due to the special structure of the antenna and its special performance in terms of beam steering capability, diverse MIMO features, high and stable gain, and circular polarization.

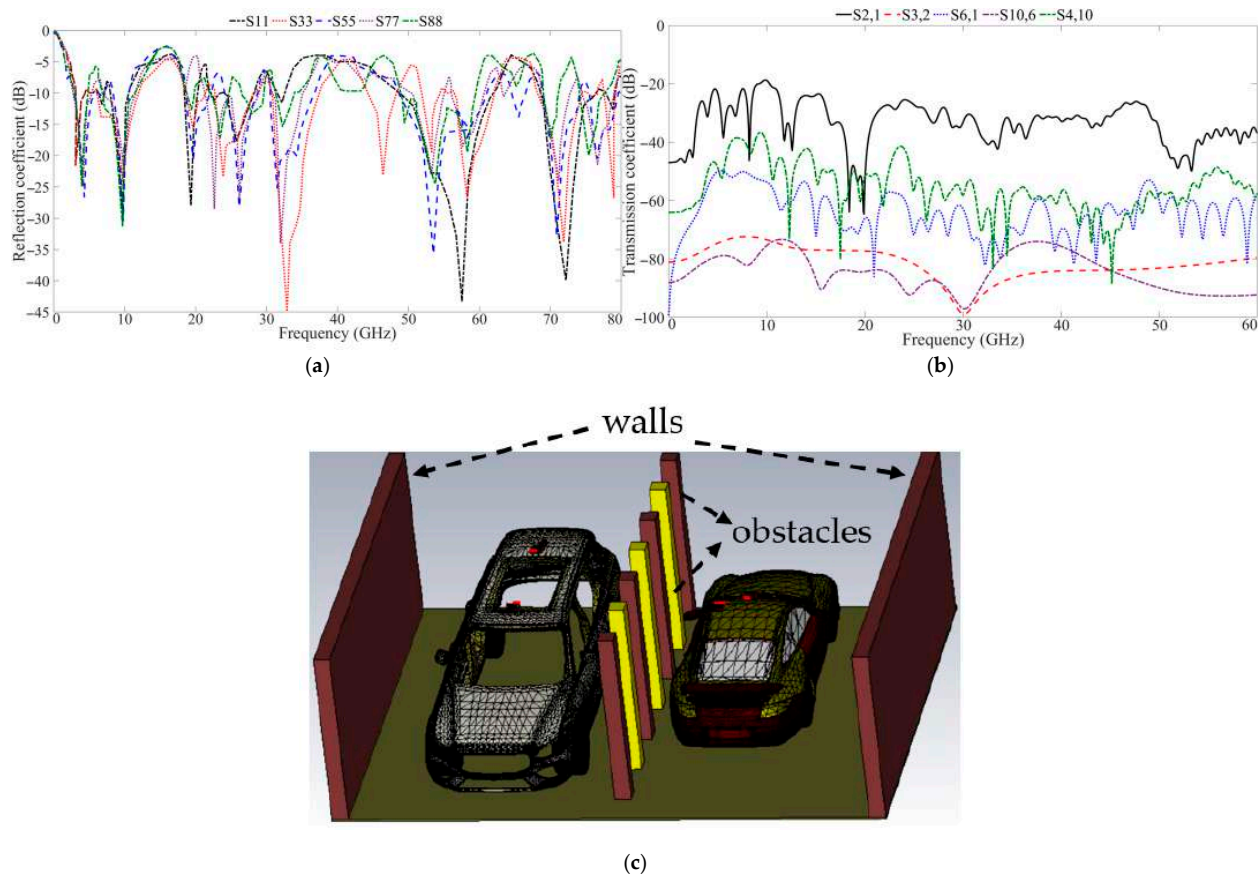


Figure 14. Simulation setup and S-parameters assessment when obstacles are between two cars and walls around the cars and soil ground beneath cars (a) reflection coefficients, (b) transmission coefficients, (c) simulation setup.

Adding two additional antennas inside the car—beyond the four antennas mounted on the roof—alters the electromagnetic environment, influencing both reflection coefficients (S_{11}) and transmission coefficients (S_{21} , S_{31} , etc.) due to increased mutual coupling and interference among antennas (Figure 15). As shown in Figure 15, the reflection coefficients (S_{11}) are affected and more stopbands are created, particularly for the newly added antennas and their neighboring antennas, as the proximity between antennas introduces additional reactive and radiative coupling effects. These interactions can create impedance mismatches as well, resulting in higher reflection levels and a narrower BW at the working bands. Similarly, the transmission coefficients (S_{21} , S_{31} , etc.) between antennas likely show increased variability due to constructive and destructive interference patterns. These patterns depend on the relative position, polarization, and resonant modes of the antennas. However, the dual-polarization feature of the antennas mitigated the coupling effects, even when close spacing slightly exceeded the acceptable thresholds of the mutual coupling levels, reducing isolation between antennas. Additionally, the presence of the car body (made of different materials like aluminum, plastic, steel, ...) is another reason for this exacerbation of BW and isolation reduction among the ports, especially for those antennas are placed in positions where the vehicle's metallic structure acts as a reflector or scatterer, creating multipath propagation. However, the special features of the antenna, such as the meander lines DGS structure, implementing neutralization networks, the combination of the leaky wave and SSPP, and the nested logarithmic spiral-like resonators, did not let the S-parameters results of the proposed antenna change dramatically. The special techniques helped maintain low reflection coefficients (<-10 dB) and high isolation (>25 dB), ensuring reliable performance in V2V, V2P, and V2I communications.

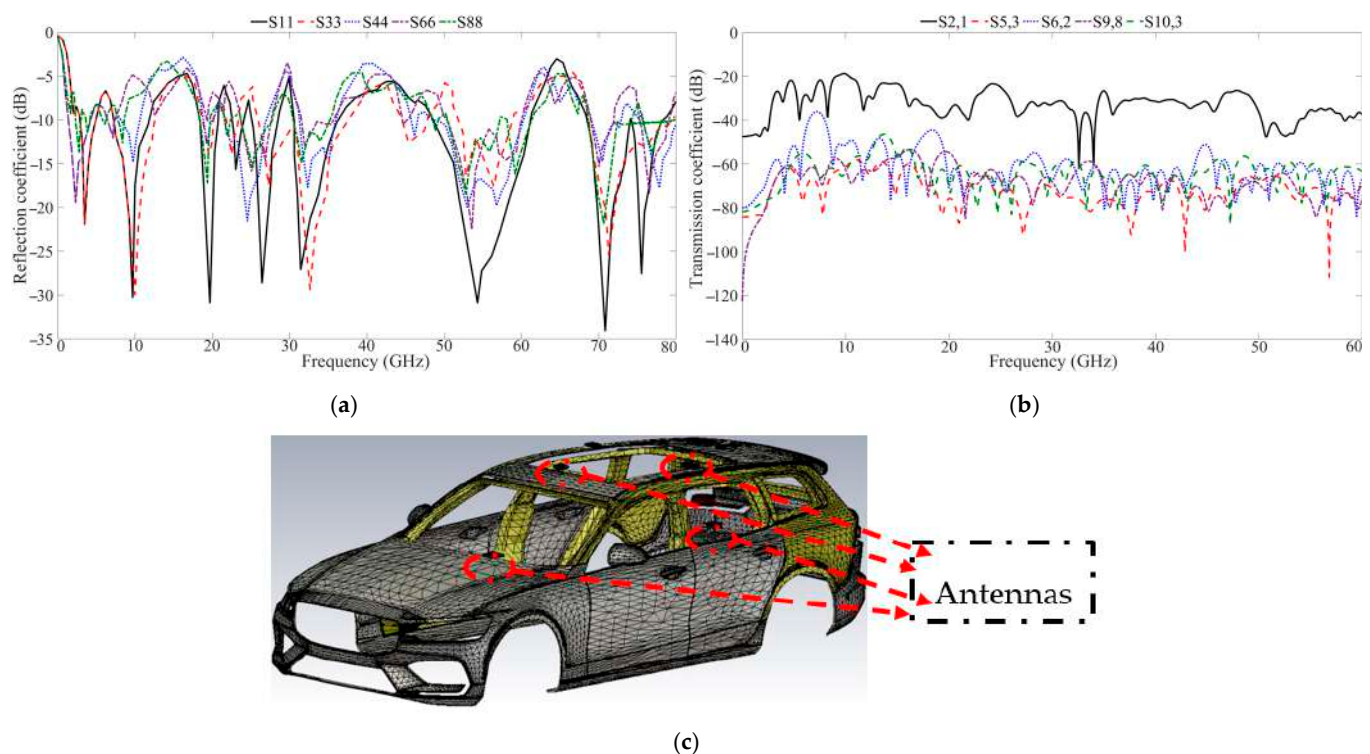


Figure 15. Simulation setup and S-parameters assessment when two antennas are inside the car for in-vehicle communications (a) reflection coefficients, (b) transmission coefficients, (c) simulation setup.

Figures 16–18 illustrate the two-dimensional radiation patterns of the proposed antenna, obtained through simulations corresponding to the scenarios depicted in Figure 12. These patterns highlight the antenna's capability to radiate in various directions, enabling

interaction with nearby vehicles, pedestrians, roadside infrastructure, and mobile network systems. The findings reveal that the antenna's positioning effectively supports V2V and V2P communications (surrounding the vehicle) as well as V2I communication (via upward radiation). The red line in the 2D patterns, representing maximum directive gain, further confirms the antenna's effectiveness.

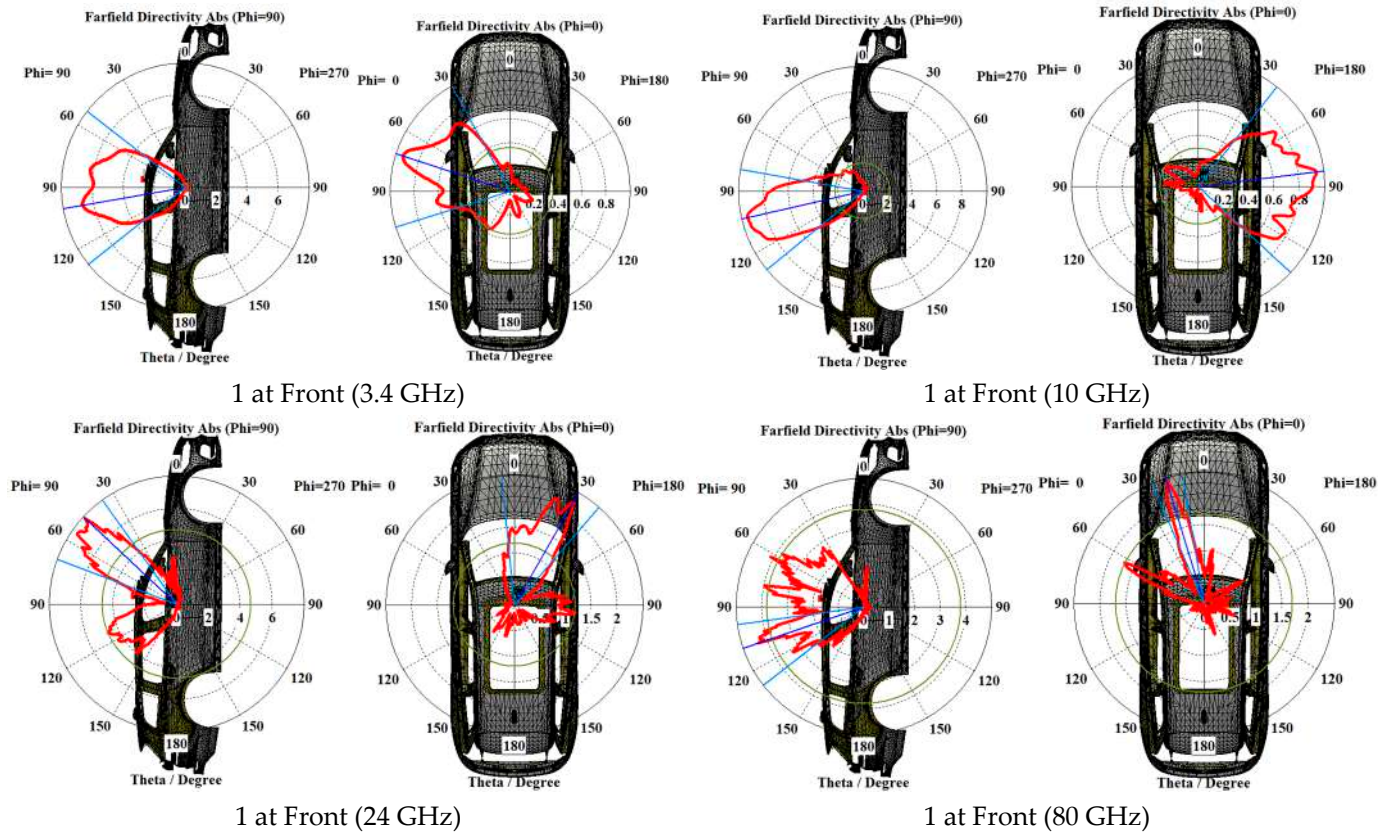


Figure 16. The two-dimensional radiation patterns of a single antenna positioned at the front.

For optimal elevation coverage, two antennas are placed on the front rooftops (Case 1), enhancing V2I and V2N communication. In Case 2, four antennas on each side of the first car's rooftop and two on the second car's sides were evaluated to identify placements that minimize coupling and reduce interference from other vehicles. Research suggests that placing antennas on all four sides (Case 3) widens the frontal visible region within the car's elevation plane, which can be achieved by mounting on the windshield with a transparent substrate to prevent obstructing the driver's view. Additionally, positioning antennas at the front and rear rooftops broadens coverage in the driver's forward field of vision, ideal for highway communication with nearby vehicles. This setup also allows for flexible antenna mounting at the front and rear edges of the rooftop in non-intrusive spots.

The radiation patterns of antennas change across different car styles, such as those with glass-dominant upper parts, due to variations in material properties, structural designs, and electromagnetic interactions. One of the reasons is the use of different materials in the car body. Cars with significant glass coverage have a higher dielectric constant and lower conductivity compared to metal parts, causing variations in electromagnetic wave propagation. Glass does not reflect radio waves as efficiently as metal but can absorb and refract them, altering the radiation patterns. In contrast, metal roofs strongly reflect and guide waves, resulting in different radiation characteristics. In addition, glass and other parts of the car create more diverse multipath effects as waves may pass through the glass, reflect from internal structures, or interact with passengers and other surfaces inside the

car. This increases back and scattered radiation, impacting directional gain and reducing efficiency in focused communication.

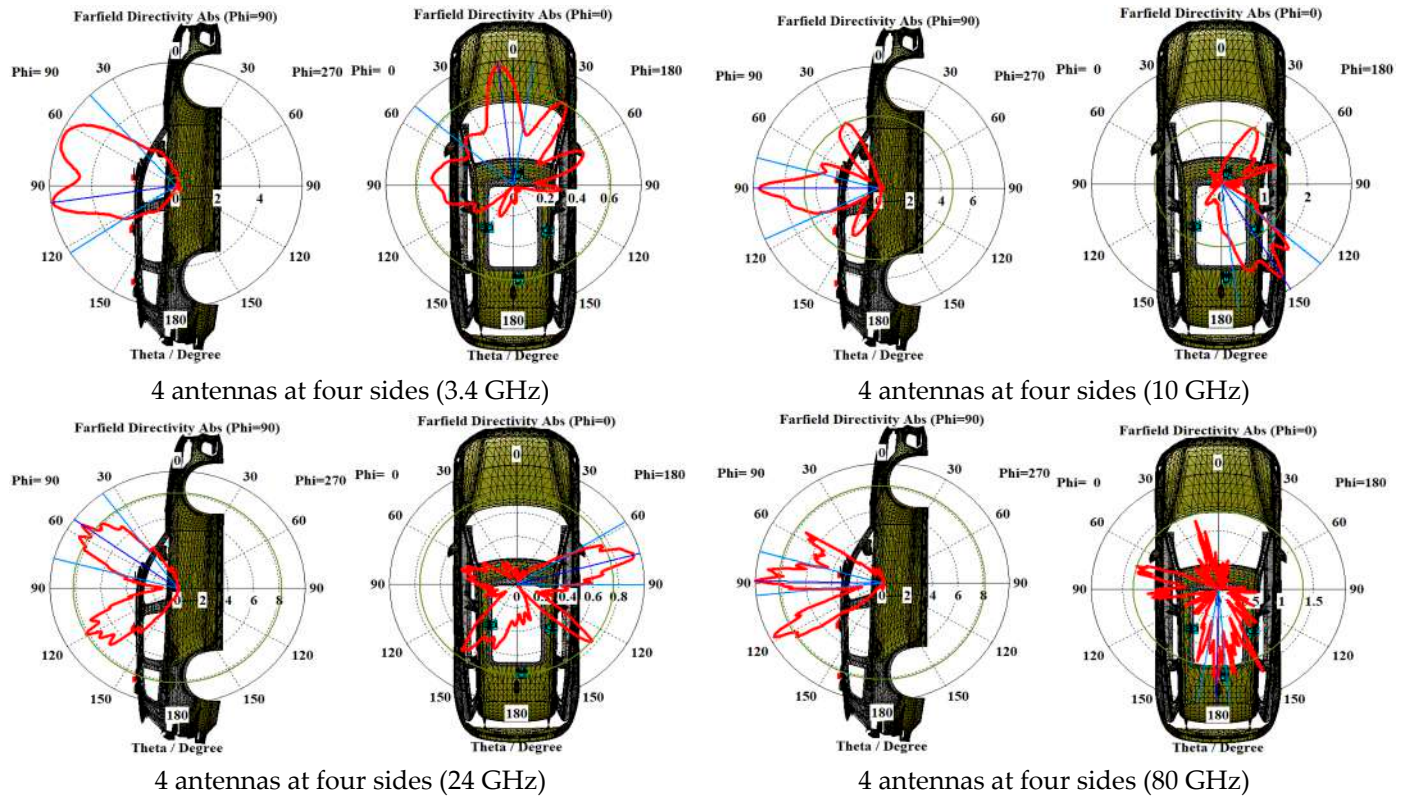


Figure 17. The two-dimensional radiation patterns when four antennas are placed on four sides.

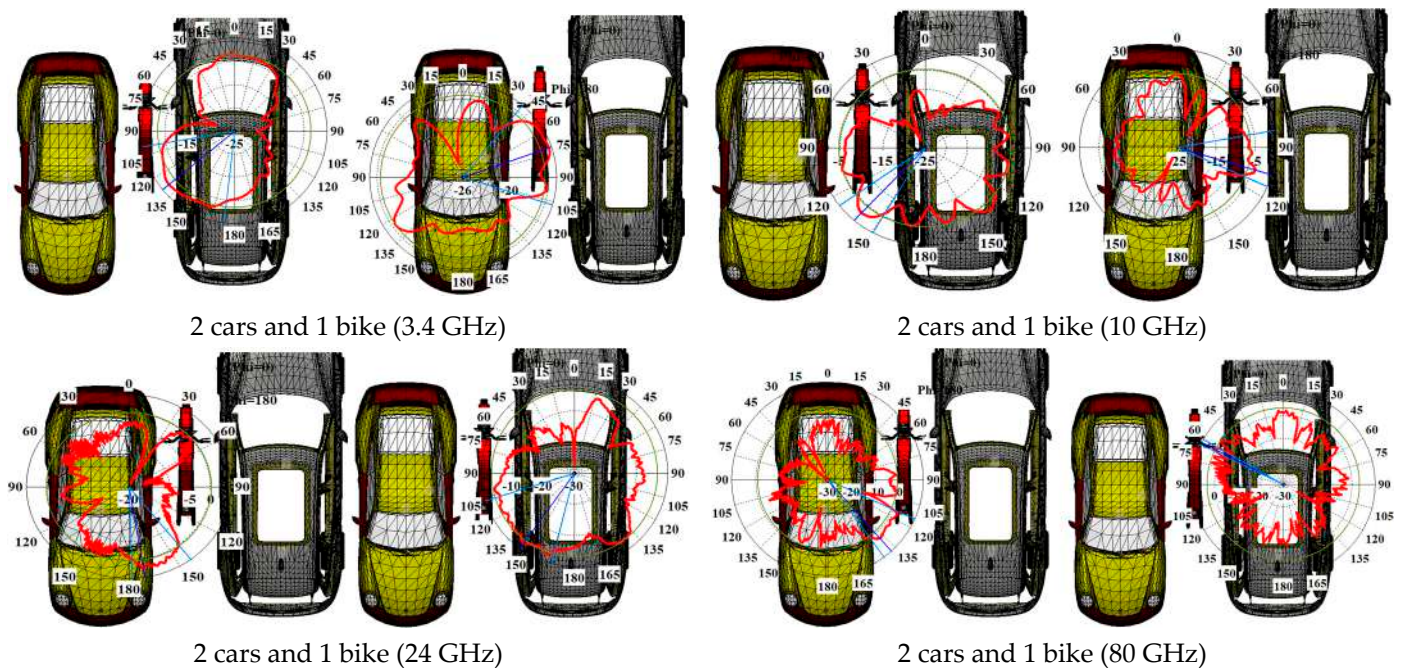


Figure 18. The two-dimensional radiation patterns with four antennas on the bigger car and two antennas on the smaller car.

Figures 16–18 compare polar radiation patterns across different configurations, including one antenna at the front, four antennas at four sides of the roof, four on the big car, and

two on the smaller car. It should be mentioned that the resented radiations are linear and directive to show which direction they are more focused on.

SAR Definition and Analysis

This part analyzes the effects of electromagnetic exposure on individuals, focusing on both drivers and pedestrians, through the evaluation of SAR. While most studies on mm-Wave V2X antennas have not accounted for this factor, this research incorporates it by simulating various scenarios with the CST voxel model (Gustav) within vehicle analyses. The findings show that electromagnetic radiation minimizes human exposure, as the vehicle body acts as a large ground plane, effectively reflecting radiation [45,46]. Three different situations are analyzed, acknowledging that roads are not always densely populated with pedestrians. The first scenario involves a driver accompanied by one passenger, while the second scenario includes four pedestrians positioned in various directions around the vehicle. SAR values for both the driver and pedestrian scenarios are provided in Tables 5 and 6, calculated with an input power of 1 W (30 dBm) and considering tissue masses of 1 g and 10 g at different resonance frequencies. The findings confirm that the SAR values comply with the safety standards established by the Federal Communications Commission (FCC) and the Council of the European Union, remaining below the allowable limit of 1.

Table 5. Evaluation of SAR with two passengers positioned in the vehicle (The red and dark-blue colors are maximum and minimum).

f_r (GHz)	1 g	10 g
3.4		
8.5		
28		

Table 5. Cont.

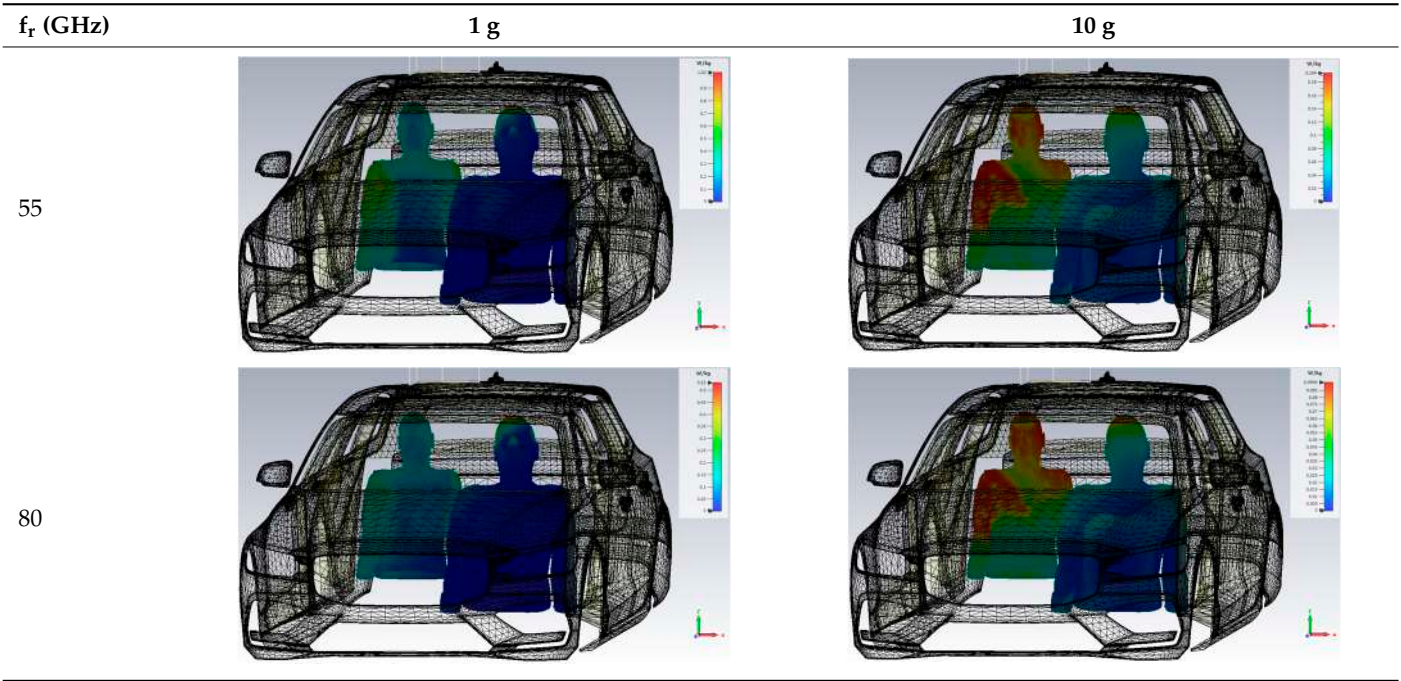
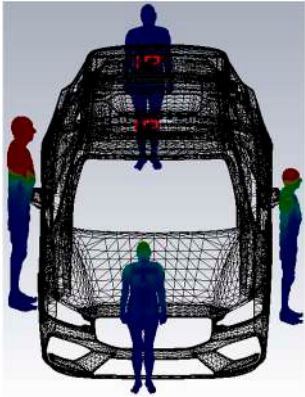



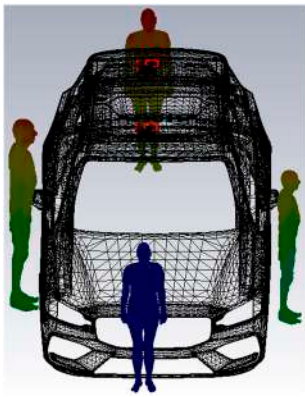



Table 6. Assessment of SAR with four pedestrians of varying ages and sizes positioned around the vehicle.



Table 6. Cont.

fr (GHz)	1 g	10 g
28		
55		
80		

4. Experimental Confirmation and Analysis of Findings

For the measurement shown in Figure 19, the setup is specifically designed to measure key performance metrics such as S-parameters (reflection and transmission coefficients) and radiation patterns of the antenna. The VNA and the anechoic chamber are complementary tools in this process, each serving distinct purposes. The R&S® ZVA67 VNA is used to measure the S-parameters, which provide insight into the impedance matching and transmission characteristics of the antenna. The VNA is connected to the antenna under test (AUT) using coaxial cables or waveguides, depending on the frequency range. Calibration is performed before measurement to remove the effects of cables and connectors, ensuring accurate results. The S11 parameter (reflection coefficient) is measured by sending a signal from one port of the VNA to the antenna and recording the reflected signal, indicating how much power is reflected due to impedance mismatch. Similarly, the S21 parameter (transmission coefficient) can be measured by analyzing the power transmitted between two

ports, which is useful in multi-port antenna systems. These measurements are conducted over the antenna's operational frequency range, up to 70 GHz, leveraging the VNA's wide dynamic range to capture the antenna's performance across multiple bands.

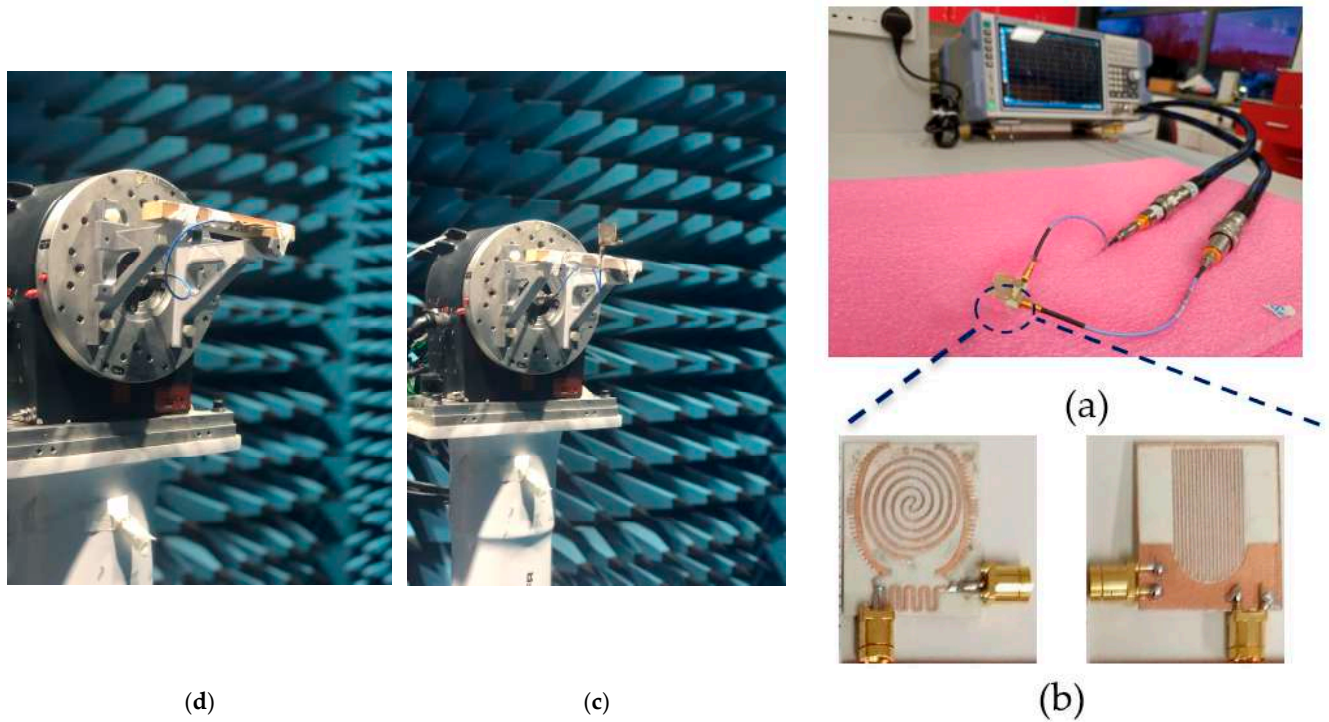


Figure 19. Measurement setup of the proposed antenna: (a) measurement setup of antenna and the network analyzer, (b) the front and back of fabricated antenna, (c) E-radiation measurement in the chamber, and (d) H-radiation measurement in the chamber.

The radiation pattern measurements are conducted in the anechoic chamber (dimensions: 10 m × 6 m × 6 m) to ensure an interference-free and reflection-free environment. The chamber is lined with radio-frequency (RF) absorbers that minimize reflections and emulate free-space conditions. The AUT is mounted on a turntable, which rotates to capture the antenna's radiation characteristics in various angular positions. A calibrated horn antenna or another reference antenna is used as a transmitter or receiver. When measuring the far-field radiation pattern, the distance between the AUT and the receiving antenna is set according to the far-field criteria. The chamber setup enables the measurement of gain, beamwidth, side-lobe levels, and polarization. By rotating the AUT or varying the measurement angles, 2D and 3D radiation patterns are obtained, providing a comprehensive understanding of the antenna's directional properties. This combination of precise S-parameter and radiation pattern measurements ensures a thorough performance evaluation of the proposed antenna.

Although the proposed antenna is compact, it exhibits excellent impedance matching across the targeted frequency ranges, as shown in Figure 20a. Specifically, it achieves reflection coefficients of less than −14.6 dB within the range of 3.32–4.28 GHz, under −12.3 dB between 8.45 and 11.7 GHz, below −11.34 dB from 16.66 to 18.45 GHz, under −15.6 dB in the 23.67–27.26 GHz range, less than −14.34 dB between 31.67 and 34.57 GHz, below −13.23 dB from 52.3 to 61.67 GHz, and between 71.8 and 82.5 GHz. This impressive performance positions the antenna as a highly suitable option for 5G mm-wave vehicular communication applications. The antenna also shows an ideal range of less than −20 dB for mutual coupling between ports and a good agreement between the simulated and measured results. Therefore, the antenna offers high isolation for MIMO communications

(Figure 20a). Additionally, as depicted in Figure 20b, the MIMO SSPP LWA achieves a measured peak gain of 11.24 dBi, a maximum radiation efficiency of 91%, and an axial ratio (AR) of 2.7 throughout the entire target operating bandwidth. The discrepancies between the simulated and measured results are attributed to fabrication tolerances, human errors, imperfect soldering of SMA connectors, and differences between simulation and real-world measurement environments.

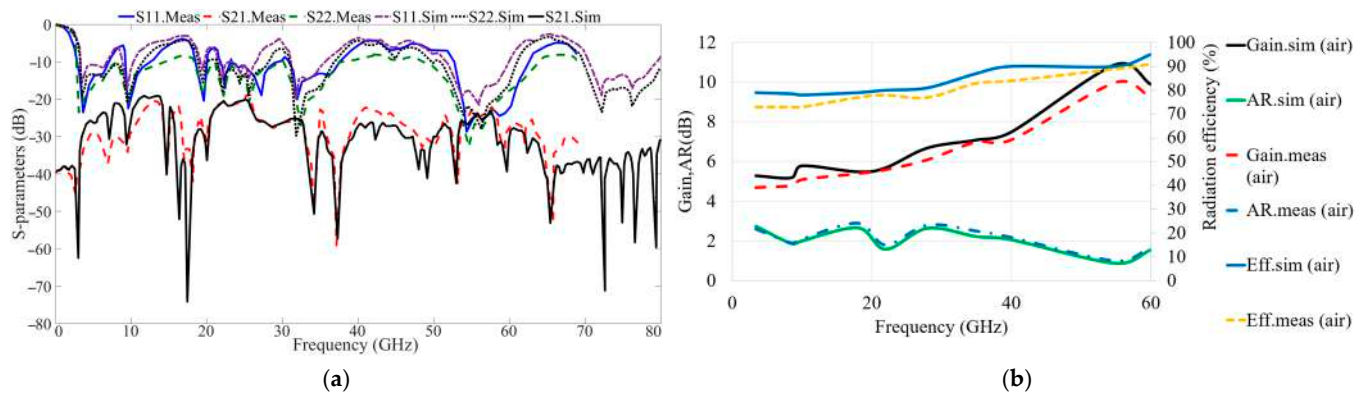


Figure 20. Observed and modeled (a) reflection and transmission parameters and (b) radiation characteristics.

Figure 21 illustrates both the simulated and measured co- and cross-polarization of the antenna. A minimal and insignificant difference was observed in the radiation measurements, attributed to potential tolerances during the manufacturing process. In addition, the cross-polarization of the antenna is less than -35 dB for all the working bands of the antenna.

The performance of the proposed MIMO antenna in terms of diversity parameters is evaluated using ECC, CCL, Mean Effective Gain (MEG), and DG, as illustrated in Figure 22. The results indicate that the antenna achieves an ECC value of less than 0.08 across the entire operational frequency range. While an ideal ECC is zero, the proposed design closely approaches this ideal. The figure also presents the DG, showing that the antenna maintains DG values exceeding 9.8 dB throughout the operational bandwidth. Additionally, the MIMO antenna demonstrates a CCL of less than 0.05 bits/Hz/s, which is well within the acceptable range. The MEG, shown in Figure 22b, reaches a maximum of -4 dB. These findings establish the proposed dual-port MIMO antenna as a strong candidate for future microwave and millimeter-wave applications.

Table 7 presents a comparison between the proposed antenna and recent related studies, highlighting that the MIMO SSPP LWA is more compact than the LWAs discussed in [1,6] (single-element) and [47]. Moreover, the proposed antenna provides a wider bandwidth than those in [1] (single-element) and [47] despite these studies potentially achieving higher gain. However, the larger size of these antennas makes them less appropriate for integration into vehicle structures. The compact nature of the proposed design, along with its broad bandwidth and high gain, ensures the required high-speed, high data rate, and low-latency performance for efficient vehicular communication. Although the antennas proposed in [9,14] utilize smaller volumes by omitting a dielectric substrate, they may not be ideal for vehicle body placement, which demands antennas with physical solid durability. In such situations, adding a cavity or communication module may be necessary, increasing the antenna's size and potentially reducing its coverage.

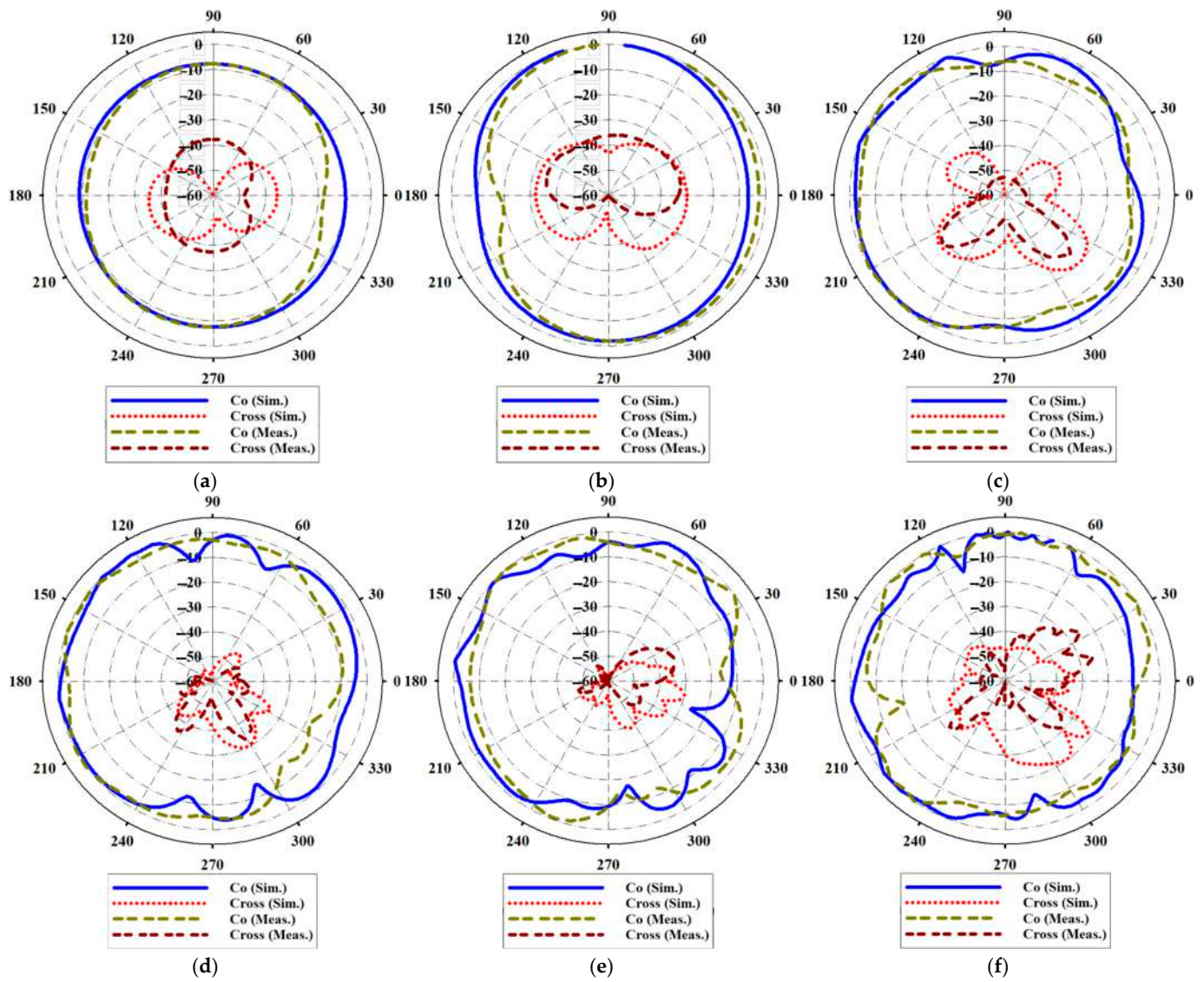


Figure 21. Measured and simulated radiation patterns of the proposed antenna at (a): 3.4 GHz, (b): 8.5 GHz, (c): 24 GHz, (d): 35 GHz, (e): 60 GHz, and (f): 80 GHz.

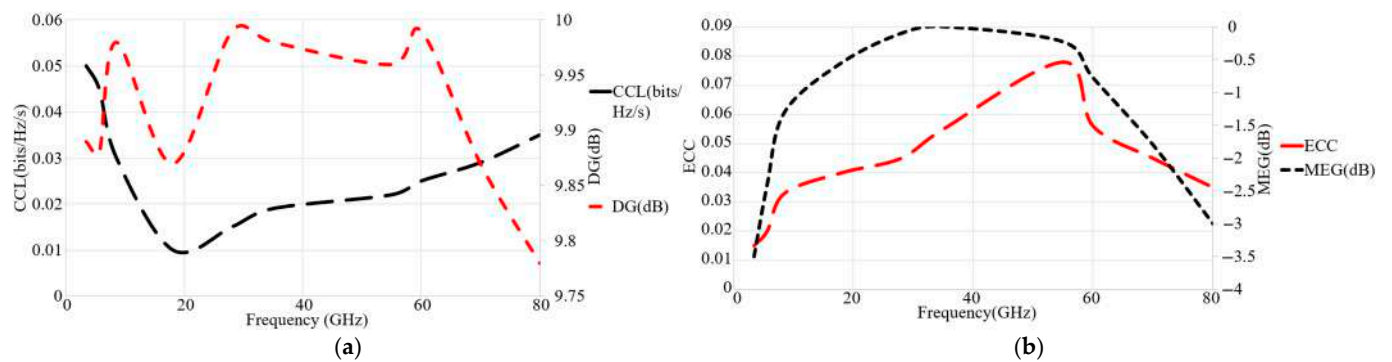


Figure 22. MIMO antenna's diversity characteristics: (a) CCL and DG, (b) ECC and MEG.

Table 7. Other related multi-band mm-wave antennas and mm-wave MIMO LWAs for vehicular communications.

Ref.	BW (GHz)	Polarization	Max. Gain (dBi)	Max. Efficiency (%)	Enhancement Techniques	Dim (mm × mm)	Applications
[1]	25.99–31.49, 5.5	N/A	8.48	93.8	Parasitic elements and corrugations	33.83 × 16	Directional 5G communication, imaging, or sensing
[5,7]	25.13–37.74, 12.61	N/A	11.13	78	Corrugations and metamaterials	14 × 33	5G communications
[14]	2.45, 2.6, 3.4, 28	Multi	9	N/A	Tapered slot antenna (TSA)	>60 Diam	5G-V2X
[24]	28	N/A	6.2	39	mm-wave on-glass antenna	25 × 25	Vehicular
[33]	11–16	N/A	12	>88	SSPP LWA, hole-shaped SSPP TL	200 × 30	Imaging radar
[34]	6–15	N/A	12	95	SSPP LWA	404 × 80	Planarly integrated communication systems
[47]	55–66, 11	N/A	14.86	90.2	DSVA, corrugations, and grating elements	70 × 40	High-speed 5G communications
[48]	16.5–18	CP/LP	12.54	98.5	Half-mode substrate-integrated waveguide LWA	170 × 35	Vehicular
[49]	56.3–63.4	CP	13.47	>62	Single layer SIW	320 × 20	V2V
[50]	24.6–42.1, 50.1–52.5	N/A	6.72	98.7	Collinear planar	22 × 13	V2X
[51]	2.6, 3.9, 5.6	N/A	5.9	N/A	U-shaped structure	120 × 120	Vehicular
[52]	27.5–32	N/A	<15	<90	SSPP	65 × 20	5G applications
[53]	8–14	N/A	<8	N/A	SSPP	269 × 63.24	Computer vision aids, VC
[54]	8–12	N/A	<10	<95	SSPP	55 × 30	Localization in X-band
[55]	4–6.5	N/A	8.5	N/A	CPW SSPP	120 × 87.5	Beyond fifth generation
This work	3.32–4.28 8.45–11.7 16.66–18.45 23.67–27.26 31.67–34.57 52.3–61.67 71.8–82.5	CP, Dual	11.6, 14.5 on car	<92	LWA SSPP	14 × 12	5G, B5G, and vehicular communication

5. Conclusions

This study demonstrates the development and effectiveness of a compact and innovative SSPP-TL MIMO leaky wave antenna (LWA) with orthogonal feeding optimized for vehicular communication applications in both lower and mm-wave 5G frequency bands. By integrating key design elements, including periodic SSPP arrays, spiral-shaped parasitic semi-circular strip patches, and a defected ground structure (DGS) with meander lines, the proposed antenna operates as a multi-band system, supporting four distinct radiation modes while significantly minimizing back and end-fire radiation. The antenna achieves exceptional reflection coefficient values ($S_{11} < -14.3$ dB) across a wide range of frequencies: 3.32–4.28 GHz, 8.45–11.7 GHz, 16.66–18.45 GHz, 23.67–27.26 GHz, 31.67–34.57 GHz, 52.3–61.67 GHz, and 71.8–82.5 GHz. With stable broadside radiation patterns, peak gains of 11.6 dBi in air and 14.5 dBi on a vehicle, and maximum radiation efficiencies of 91% and 93%, respectively, this antenna demonstrates outstanding beam-steering and dual-polarization capabilities. The compact size ($14 \times 12 \times 0.25$ mm³) further highlights its suitability for integration into modern connected and autonomous vehicles. Extensive testing confirms its robust performance across various vehicular scenarios, supporting Vehicle-to-Vehicle (V2V), Vehicle-to-Pedestrian (V2P), and Vehicle-to-Infrastructure (V2I) communication. Additionally, the Specific Absorption Rate (SAR) values for drivers and pedestrians remain well within the safety limits set by regulatory authorities, ensuring safe electromagnetic exposure. This work underscores the transformative potential of integrating SSPP structures with leaky wave antennas to enable compact, multi-functional, and high-performing designs for vehicular communication. The proposed antenna provides seamless connectivity with mobile networks and ensures reliable communication with surrounding vehicles, pedestrians, and roadside units, addressing critical challenges in modern automotive communication networks. Future research can explore the integration of this antenna into larger vehicular networks with dynamic beamforming and adaptive MIMO configurations, further enhancing its utility in congested urban environments and complex vehicular communication scenarios. Additionally, optimizing the antenna for multi-protocol support, such as 5G, Wi-Fi 6E, and satellite communication, could expand its applications for connected and autonomous vehicles. Investigating materials with higher mechanical robustness and environmental resilience will also facilitate their deployment in harsh vehicular environments. These advancements will ensure that the proposed antenna remains at the forefront of vehicular communication technologies, driving the evolution of next-generation intelligent transportation systems.

Author Contributions: T.S. wrote the original draft of the paper, designed the structure, and carried out the simulation and measurement. S.S., N.T. and S.K. edited the paper and evaluated the antenna's performance. A.J.A.A.-G. and F.R. edited the paper and carried out the investigations. Finally, C.M. did the fabrication and investigations. All authors have read and agreed to the published version of the manuscript.

Funding: This research was funded by Enterprise Ireland.

Institutional Review Board Statement: Not applicable.

Informed Consent Statement: Not applicable.

Data Availability Statement: Data are contained within the article.

Acknowledgments: Enterprise Ireland supported this work.

Conflicts of Interest: The authors declare no conflicts of interest.

References

1. Mahmood, D.A.; Reja, A.H.; Mahmood, A.M. Enhancement of information propagation on the highway in VANET based on Multiple Vehicle Class. In Proceedings of the International Conference on ICT Convergence 2022, Jeju Island, Republic of Korea, 19–21 October 2022; pp. 1419–1424. [\[CrossRef\]](#)
2. Ström, E.G.; Ekiz, L.; Abbas, T.; He, R.; Ambroziak, S.J.; Shivaldova, V.; Nuckelt, J. Vehicular communication environments. In *Cooperative Radio Communications for Green Smart Environments*; River Publishers: Roma, Italy, 2016; pp. 121–150. [\[CrossRef\]](#)
3. Ghafoor, K.Z.; Kong, L.; Zeadally, S.; Sadiq, A.S.; Epiphaniou, G.; Hammoudeh, M.; Bashir, A.K.; Mumtaz, S. Millimeter-wave Communication for Internet of Vehicles: Status, Challenges and Perspectives. *IEEE Internet Things J.* **2020**, *7*, 8525–8546. [\[CrossRef\]](#)
4. Pirayesh, H.; Zeng, H. Jamming Attacks and Anti-Jamming Strategies in Wireless Networks: A Comprehensive Survey. *IEEE Commun. Surv. Tutor.* **2022**, *24*, 767–809. [\[CrossRef\]](#)
5. Giordani, M.; Zanella, A.; Zorzi, M. Millimeter wave communication in vehicular networks: Challenges and opportunities. In Proceedings of the 2017 6th International Conference on Modern Circuits and Systems Technologies (MOCAS), Thessaloniki, Greece, 4–6 May 2017; pp. 1–6.
6. Na, W.; Lakew, S.; Lee, J.; Cho, S. Congestion control vs. link failure: TCP behavior in mmWave connected vehicular networks. *Future Gener. Comput. Syst.* **2019**, *101*, 1213–1222. [\[CrossRef\]](#)
7. Pons, M.; Valenzuela, E.; Rodríguez, B.; Nolasco-Flores, J.A.; Del-Valle-Soto, C. Utilization of 5G Technologies in IoT Applications: Current Limitations by Interference and Network Optimization Difficulties—A Review. *Sensors* **2023**, *23*, 3876. [\[CrossRef\]](#)
8. Saleh, S.; Saeidi, T.; Timmons, N.; Razzaz, F. A comprehensive review of recent methods for compactness and performance enhancement in 5G and 6G wearable antennas. *Alex. Eng. J.* **2024**, *95*, 132–163. [\[CrossRef\]](#)
9. Nasr, A.M.H.; Sarabandi, K. A Low-Cost Millimeter-Wave 5G V2X Multi-Beam Dual-Polarized Windshield Antenna. *IEEE Open J. Antennas Propag.* **2022**, *3*, 1313–1323. [\[CrossRef\]](#)
10. Ballesteros, C.; Montero, L.; Ramírez, G.A.; Jofre-Roca, L. Multi-antenna 3D pattern design for millimeter-wave vehicular communications. *Veh. Commun.* **2022**, *35*, 100473. [\[CrossRef\]](#)
11. Dzagbletey, P.A.; Shim, J.; Chung, J. Quarter-Wave Balun Fed Vivaldi Antenna Pair for V2X Communication Measurement. *IEEE Trans. Antennas Propag.* **2019**, *67*, 1957–1962. [\[CrossRef\]](#)
12. Bonato, M.; Tognola, G.; Benini, M.; Gallucci, S.; Chiamello, E.; Focchi, S.; Parazzini, M. Assessment of SAR in Road-Users from 5G-V2X Vehicular Connectivity Based on Computational Simulations. *Sensors* **2022**, *22*, 6564. [\[CrossRef\]](#) [\[PubMed\]](#)
13. Kim, W. Experimental Demonstration of MmWave Vehicle-to-Vehicle Communications Using IEEE 802.11ad. *Sensors* **2019**, *19*, 2057. [\[CrossRef\]](#)
14. Ikram, M.; Sultan, K.S.; Abbosh, A.M.; Nguyen-Trong, N. Sub-6 GHz and mm-Wave 5G Vehicle-to-Everything (5G-V2X) MIMO Antenna Array. *IEEE Access* **2022**, *10*, 49688–49695. [\[CrossRef\]](#)
15. Im, C.; Lim, T.H.; Jang, D.; Kong, N.K.; Choo, H. Design of a printed 5G monopole antenna on vehicle window glass using parasitic elements and a lattice-structure reflector for gain enhancement. *Appl. Sci.* **2021**, *11*, 9953. [\[CrossRef\]](#)
16. Sun, Y.X.; Leung, K.W.; Lu, K. Compact Dual Microwave/Millimeter-Wave Planar Shared-Aperture Antenna for Vehicle-to-Vehicle/5G Communications. *IEEE Trans. Veh. Technol.* **2021**, *70*, 5071–5076. [\[CrossRef\]](#)
17. Ding, X.H.; Yang, W.W.; Tang, H.; Guo, L.; Chen, J.X. A Dual-Band Shared-Aperture Antenna for Microwave and Millimeter-Wave Applications in 5G Wireless Communication. *IEEE Trans. Antennas Propag.* **2022**, *70*, 12299–12304. [\[CrossRef\]](#)
18. Wang, C.; Cao, W.; Ma, W.; Tong, Y.; Zhu, Y. A Single-Layer Dual-Band Shared-Aperture Antenna With High Gain and Sidelobe Suppression Based on High-Order Mode for Vehicular Communications. *IEEE Trans. Veh. Technol.* **2023**, *73*, 473–481. [\[CrossRef\]](#)
19. Xu, S.-D.; Guan, D.-F.; Zhang, Q.; You, P.; Ge, S.; Hou, X.-X.; Yang, Z.-B.; Yong, S.-W. A Wide-Angle Narrowband Leaky-Wave Antenna Based on Substrate Integrated Waveguide-Spoof Surface Plasmon Polariton Structure. *IEEE Antennas Wirel. Propag. Lett.* **2019**, *18*, 1386–1389. [\[CrossRef\]](#)
20. Ren, B.; Li, W.; Qin, Z.; Wang, Y.; Zhang, L.; Zhang, B. Leaky Wave Antenna Based on Periodically Truncated SSPP Waveguide. *Plasmonics* **2020**, *15*, 551–558. [\[CrossRef\]](#)
21. Bryant, B.; Won, H.; Hong, Y.K.; Lee, W.; Choi, M. Design of Triple-Band (DSRC, 5G, 6G) Antenna for Autonomous Vehicle Telematics. *Electronics* **2022**, *11*, 2523. [\[CrossRef\]](#)
22. Rao, M.V.; Madhav, B.T.P.; Krishna, J.; Devi, Y.U.; Anilkumar, T.; Nadh, B.P. CSRR-loaded T-shaped MIMO antenna for 5G cellular networks and vehicular communications. *Int. J. RF Microw. Comput.-Aided Eng.* **2019**, *29*, e21799. [\[CrossRef\]](#)
23. Jang, D.; Kong, N.K.; Choo, H. Design of an On-Glass 5G Monopole Antenna for a Vehicle Window Glass. *IEEE Access* **2021**, *9*, 152749–152755. [\[CrossRef\]](#)
24. Im, C.; Lim, T.H.; Choo, H. Design of a mmWave Antenna Printed on a Thick Vehicle-Glass Substrate Using a Linearly Arrayed Patch Director and a Grid-Slotted Patch Reflector for High-Gain Characteristics. *Sensors* **2022**, *22*, 6187. [\[CrossRef\]](#) [\[PubMed\]](#)
25. Youn, S.; Jang, D.; Kong, N.K.; Choo, H. Design of a Printed 5G Monopole Antenna with Periodic Patch Director on the Laminated Window Glass. *IEEE Antennas Wirel. Propag. Lett.* **2022**, *21*, 297–301. [\[CrossRef\]](#)

26. Tan, H.; Zheng, W.; Vijayakumar, P. Secure and Efficient Authenticated Key Management Scheme for UAV-Assisted Infrastructure-Less IoVs. *IEEE Trans. Intell. Transp. Syst.* **2023**, *24*, 6389–6400. [\[CrossRef\]](#)
27. Liu, P.; He, Q.; Chen, Y.; Jiang, S.; Zhao, B.; Wang, X. A Lightweight Authentication and Privacy-Preserving Aggregation for Blockchain-Enabled Federated Learning in VANETs. *IEEE Trans. Consum. Electron.* **2024**; *Early Access*.
28. Pan, X.; Jin, Y.; Li, F. An efficient heterogeneous authenticated key agreement scheme for unmanned aerial vehicles. *J. Syst. Arch.* **2023**, *136*, 102821. [\[CrossRef\]](#)
29. Nandy, T.; Idris, M.Y.I.; Noor, R.M.; Wahab, A.W.A.; Bhattacharyya, S.; Kolandaisamy, R. A Secure, Privacy-Preserving, and Lightweight Authentication Scheme for VANETs. *IEEE Sens. J.* **2021**, *21*, 20998–21011. [\[CrossRef\]](#)
30. Li, C.-T.; Weng, C.-Y.; Chen, C.-L.; Lee, C.-C.; Deng, Y.-Y.; Imoize, A.L. An Efficient Authenticated Key Agreement Scheme Supporting Privacy-Preservation for Internet of Drones Communications. *Sensors* **2022**, *22*, 9534. [\[CrossRef\]](#) [\[PubMed\]](#)
31. Gu, Z.; Ma, Q.; Gao, X.; You, J.W.; Cui, T.J. Direct electromagnetic information processing with planar diffractive neural network. *Sci. Adv.* **2024**, *10*, eado3937. [\[CrossRef\]](#) [\[PubMed\]](#)
32. Gao, X.X.; Ma, Q.; Gu, Z.; Cui, W.Y.; Liu, C.; Zhang, J.J.; Cui, T.J. Programmable surface plasmonic neural networks for microwave detection and processing. *Nat. Electron.* **2023**, *6*, 319–328. [\[CrossRef\]](#)
33. Ali, S.M.; Jeoti, V.; Saeidi, T.; Wen, W.P. Design of compact microstrip patch antenna for WBAN applications at ISM 2.4 GHz. *Indones. J. Electr. Eng. Comput. Sci.* **2019**, *15*, 1509–1516.
34. Kumar, R.; Dhubbakarya, D.C. Design and Analysis of Circular Ring Microstrip Antenna. *Glob. J. Res. Eng.* **2011**, *11*, 1–5.
35. Zhu, A.q.; Liao, X.; Wang, B.; Pen, L.; Cheng, L.; Liu, Y.; Jiang, X. Compact spoof surface plasmon polariton leaky-wave antenna with consistent gain. *Microw. Opt. Technol. Lett.* **2021**, *63*, 2430–2435. [\[CrossRef\]](#)
36. Liu, L.; Chen, M.; Cai, J.; Yin, X.; Zhu, L. Single-Beam Leaky-Wave Antenna With Lateral Continuous Scanning Functionality Based on Spoof Surface Plasmon Transmission Line. *IEEE Access* **2019**, *7*, 25225–25231. [\[CrossRef\]](#)
37. Zhang, Q.L.; Zhang, Q.; Chen, Y. Spoof Surface Plasmon Polariton Leaky-Wave Antennas using Periodically Loaded Patches above PEC and AMC Ground Planes. *IEEE Antennas Wirel. Propag. Lett.* **2017**, *16*, 3014–3017. [\[CrossRef\]](#)
38. Alibakhshikenari, M.; Virdee, B.S.; See, C.H.; Abd-Alhameed, R.A.; Falcone, F.; Limiti, E. High-Isolation Leaky-Wave Array Antenna Based on CRLH-Metamaterial Implemented on SIW with $\pm 30^\circ$ Frequency Beam-Scanning Capability at Millimetre-Waves. *Electronics* **2019**, *8*, 642. [\[CrossRef\]](#)
39. Saeidi, T.; Saleh, S.; Mahmood, S.N.; Timmons, N.; Al-Gburi, A.J.A.; Karamzadeh, S.; Razzaz, F. High gain multi-band circularly polarized wearable leaky wave zipper MIMO antenna. *Heliyon* **2024**, *10*, e33024. [\[CrossRef\]](#)
40. Saeidi, T.; Saleh, S.; Timmons, N.; Al-Gburi, A.J.A.; Karamzadeh, S.; Althuwayb, A.A.; Rashid, N.; Kaaniche, K.; Atitallah, A.B.; Elhamrawy, O.I. Meta Surface-Based Multi-band MIMO Antenna for UAV Communications at mm-Wave and Sub-THz Bands. *Drones* **2024**, *8*, 403. [\[CrossRef\]](#)
41. Zohrevand, S.; Zadeh, M.A.C.; Farokhipour, E.; Erni, D.; Komjani, N. Holographic inspired high-performance circular polarized spoof surface plasmon polariton leaky-wave antenna excited by a novel launcher. *Sci. Rep.* **2025**, *15*, 1149. [\[CrossRef\]](#)
42. Chen, J.; Yuan, W.; Tang, W.X.; Wang, L.; Cheng, Q.; Cui, T.J. Linearly Sweeping Leaky-Wave Antenna With High Scanning Rate. *IEEE Trans. Antennas Propag.* **2021**, *69*, 3214–3223. [\[CrossRef\]](#)
43. Car—STEP/IGES, Automotive—Recent Models | 3D CAD Model Collection | GrabCAD Community Library. Available online: https://grabcad.com/library/software/step-slash-iges?page=1&time=all_time&sort=recent&categories=automotive&query=car (accessed on 19 May 2024).
44. Available online: <https://free3d.com/3d-models/obj-car> (accessed on 20 November 2019).
45. Artner, G.; Kotterman, W.; Del Galdo, G.; Hein, M.A. Automotive Antenna Roof for Cooperative Connected Driving. *IEEE Access* **2019**, *7*, 20083–20090. [\[CrossRef\]](#)
46. Ko, M.; Lee, H.; Choi, J. Planar LTE/sub-6 GHz 5G MIMO antenna integrated with mmWave 5G beamforming phased array antennas for V2X applications. *IET Microw. Antennas Propag.* **2020**, *14*, 1283–1295. [\[CrossRef\]](#)
47. Mohammad, Z.; Sarker, N.; Das, C. Design and Analysis of a Double Slotted with Multiple Strips Vivaldi Antenna for High-Speed 5G Communications. In Proceedings of the 3rd IEEE International Conference on Telecommunications and Photonics, ICTP 2019, Dhaka, Bangladesh, 28–30 December 2019; pp. 19–22. [\[CrossRef\]](#)
48. Chen, A.; Fu, X.; Jiang, W.; An, K. Polarization-Flexible and Frequency-Scanning Leaky-Wave HMSIW Antenna for Vehicular Applications. *Electronics* **2022**, *11*, 2103. [\[CrossRef\]](#)
49. Sah, P.; Mahbub, I. A 38° Wide Beam-Steerable Compact and Highly Efficient V-band Leaky Wave Antenna with Surface Integrated Waveguide for Vehicle-to-Vehicle Communication. In Proceedings of the 2023 IEEE Texas Symposium on Wireless and Microwave Circuits and Systems (WMCS), Waco, TX, USA, 19–20 April 2023.
50. Devi, Y.U.; Boddapati, M.T.; Kumar, T.A.; Sri Kavaya Ch, K.; Pardhasaradhi, P. Conformal Printed MIMO Antenna with DGS for Millimeter Wave Communication Applications. *Int. J. Electron. Lett.* **2019**, *8*, 329–343. [\[CrossRef\]](#)
51. Saritha, V.; Chandrasekhar, C. A Conformal Multi-Band MIMO Antenna for Vehicular Communications. *Prog. Electromagn. Res. Lett.* **2023**, *108*, 49–57. [\[CrossRef\]](#)

52. Zhang, X.-F.; Fan, J.; Chen, J.-X. High Gain and High-Efficiency Millimeter-Wave Antenna Based on Spoof Surface Plasmon Polaritons. *IEEE Trans. Antennas Propag.* **2019**, *67*, 687–691. [[CrossRef](#)]
53. Li, W.; Chen, J.; Gao, S.; Niu, L.; Wei, J.; Sun, R.; Wei, Y.; Tang, W.; Cui, T.J. An externally perceivable smart leaky-wave antenna based on spoof surface plasmon polaritons. *Opto-Electron. Adv.* **2024**, *7*, 240040. [[CrossRef](#)]
54. Kandwal, A.; Li, J.; Igbe, T.; Liu, Y.; Li, S.; Wang, L.; Hao, Y.; Nie, Z. Broadband Frequency Scanning Spoof Surface Plasmon Polariton Design with Highly Confined Endfire Radiations. *Sci. Rep.* **2020**, *10*, 113. [[CrossRef](#)] [[PubMed](#)]
55. Sonagara, A.M.; Mishra, M.; Kshetrimayum, R.S.; Björnson, E.; Chen, Z.N. Ultra-Thin Flexible Uniplanar Antenna Based on SSPP for B5G Radio Stripe Network. *IEEE Antennas Wirel. Propag. Lett.* **2023**, *22*, 1947–1951. [[CrossRef](#)]

Disclaimer/Publisher’s Note: The statements, opinions and data contained in all publications are solely those of the individual author(s) and contributor(s) and not of MDPI and/or the editor(s). MDPI and/or the editor(s) disclaim responsibility for any injury to people or property resulting from any ideas, methods, instructions or products referred to in the content.